Pure and Applied Geophysics

CrossMark

Dynamic In Situ Three-Dimensional Imaging and Digital Volume Correlation Analysis to Quantify Strain Localization and Fracture Coalescence in Sandstone

FRANÇOIS RENARD,[1,2] (iD) JESSICA MCBECK,[1] BENOÎT CORDONNIER,[1,3] XIAOJIAO ZHENG,[1] NEELIMA KANDULA,[1] JESUS R. SANCHEZ,[1] MAYA KOBCHENKO,[1] CATHERINE NOIRIEL,[4] WENLU ZHU,[5] PAUL MEAKIN,[6] FLORIAN FUSSEIS,[7] and DAG K. DYSTHE[1]

Abstract—Advances in triaxial compression deformation apparatus design, dynamic X-ray microtomography imaging, data analysis techniques, and digital volume correlation analysis provide unparalleled access to the in situ four-dimensional distribution of developing strain within rocks. To demonstrate the power of these new techniques and acquire detailed information about the micromechanics of damage evolution, deformation, and failure of porous rocks, we deformed 3-cm-scale cylindrical specimens of low-porosity Fontainebleau sandstone in an X-ray-transparent triaxial compression apparatus, and repeatedly recorded three-dimensional tomograms of the specimens as the differential stress was increased until macroscopic failure occurred. Experiments were performed at room temperature with confining pressure in the range of 10–20 MPa. Distinct grayscale subsets, indicative of density, enabled segmentation of the three-dimensional tomograms into intact rock matrix, pore space, and fractures. Digital volume correlation analysis of pairs of tomograms provided time series of three-dimensional incremental strain tensor fields throughout the experiments. After the yield stress was reached, the samples deformed first by dilatant opening and propagation of microfractures, and then by shear sliding via grain rotation and strain localization along faults. For two samples, damage and dilatancy occurred by grain boundary opening and then a sudden collapse of the granular rock framework at failure. For the third sample, a fault nucleated near the yield point and propagated in the sample through the development of transgranular microfractures. The results confirm findings of previous experimental studies on the same rock and provide new detailed quantifications of: (1) the proportion of shear versus dilatant strain in the sample, (2) the amount of dilatancy due to microfracture opening versus pore opening when a fault develops, and (3) the role of grain boundaries and pore walls in pinning microfracture propagation and slowing down the rate of damage accumulation as failure is approached. Our study demonstrates how the combination of high-resolution in situ dynamic X-ray microtomography imaging and digital volume image correlation analysis can be used to provide additional information to unravel brittle failure processes in rocks under stress conditions relevant to the upper crust.

Key words: Faulting, rupture nucleation, damage, dynamic X-ray microtomography, Fontainebleau sandstone, digital volume correlation.

[1] Departments of Geosciences and Physics, The Njord Centre, PGP, University of Oslo, Oslo, Norway. E-mail: francois.renard@geo.uio.no

[2] Université Grenoble Alpes, Université Savoie Mont Blanc, CNRS, IRD, IFSTTAR, ISTerre, 38000 Grenoble, France.

[3] ESRF, The European Synchrotron Radiation Facility, Grenoble, France.

[4] Géosciences Environnement Toulouse, Observatoire Midi-Pyrénées, Université de Toulouse, Université Paul Sabatier, CNRS, IRD, CNES, 14 avenue Edouard Belin, 31400 Toulouse, France.

[5] Department of Geology, University of Maryland, College Park, MD 20742, USA.

[6] Department of Physics, Temple University, Philadelphia, PA, USA.

[7] School of Geosciences, University of Edinburgh, Edinburgh EH9 3JW, UK.

1. Introduction

Acquiring detailed observations about the processes that control the propagation and coalescence of microfractures that lead to system-size failure is critical for robust understanding of borehole and tunnel stability, the geometry of fractures and faults in crustal reservoirs, and earthquake physics. Microfractures may coalesce and lead to macroscopic failure (Scholz 1968; Wawersik and Fairhurst 1970; Mogi 1971; Peng and Johnson 1972; Tapponnier and Brace 1976; Lockner et al. 1991; Dresen and Guéguen 2004; Paterson and Wong 2005), and evolving microfractures within fault damage zones alter the stress field surrounding faults (Otsuki and Dilov 2005; Faulkner et al. 2006). Fracture networks may influence fluid flow near major faults, which can

Birkhäuser

decrease the effective stress on the fault plane and lower the shear stress required to trigger an earthquake (Miller et al. 2004). In addition, growing microfracture networks that evolve as rocks approach macroscopic failure may change the mechanical properties of the rock (Heap and Faulkner 2008), upon which accurate seismic imaging of fault damage zones depends.

Many laboratory studies have relied on acoustic emission monitoring to provide insights into deformation preceding failure. This technique was the first method used to probe inside rocks during in situ deformation, and it has very successfully provided information about failure modes and the approximate spatial and temporal distribution of damage events in crystalline rocks and porous sedimentary rocks (e.g. Scholz 1968; Lockner et al. 1991, 1992; Cox and Meredith 1993; Wu et al. 2000; Stanchits et al. 2006; Fortin et al. 2009; Ghaffari et al. 2014). A limitation of using acoustic emission recording is that it only captures events that emit acoustic waves with frequencies and intensities that can be detected in the presence of background noise. Furthermore, the velocities, attenuation, scattering, and diffraction of acoustic waves depend on spatially varying heterogeneities that evolve with the developing fracture networks. Consequently, the error in the acoustic source location is on the order of several millimeters (Stanchits et al. 2006), which is typically larger than the grain size of the rock. Additional information about the acoustic source size and orientation can be obtained from moment tensor analysis (Kwiatek et al. 2014). This analysis requires high-quality data, a large number of well-calibrated and high-dynamic-range acoustic sensors, and knowledge of the elastodynamic tensor Green's function. Like other mechanical properties, the Green's function changes during fracturing, and can be accurately determined for heterogeneous materials only if its local variations can be measured. Consequently, accurate information about the fracture sizes, shapes, and orientations can be obtained from acoustic emission experiments only when high-quality and low-noise data are available and heavy data processing is performed (e.g. Kwiatek et al. 2014).

In situ three-dimensional dynamic X-ray micro-tomography imaging combined with digital volume correlation (DVC) analysis is complementary to acoustic emission tomography because it provides detailed information about the evolution of the microscopic and macroscopic strain fields at micrometer-scale spatial resolution and precision. Data may include aseismic deformation that cannot be measured by acoustic emissions. Here, we describe this recent experimental technique, discuss its potential limits, and show how it can be applied to study the initiation of faulting in rocks. We focus on the application of this technique to an experimental investigation of the microscopic deformation of three specimens of Fontainebleau sandstone under triaxial compression. Using in situ three-dimensional X-ray tomography, digital volume correlation analysis, and scaling statistics, we quantified the evolution of: (1) porosity, (2) nucleation, growth, and coalescence of microfractures, and (3) interactions between local microscopic dilation, contraction, and shear strain that leads to system-size shear failure with increasing stress. Segmentation of the three-dimensional tomograms into rock matrix, pore space, and fractures provided four-dimensional spatiotemporal information about the evolving pore space and fracture network. The results provide insights into the deformation mechanisms at the grain scale, and how small-scale strain concentrations evolved preceding macroscopic failure, confirming the results of previous studies of sandstones (Handin et al. 1963; Menéndez et al. 1996; Wu et al. 2000; El Bied et al. 2002; Schubnel et al. 2007; Nasseri et al. 2014; Goodfellow et al. 2015). In addition, digital volume correlation analysis enabled calculation of the three-dimensional incremental strain fields between successive tomograms at a strain resolution one order of magnitude higher than the imaging resolution. Information about the magnitude and distribution of local volumetric and shear strains preceding failure was used to determine the probability density distribution of the incremental strain magnitudes. Combining analysis of segmented three-dimensional tomograms with DVC analysis improved our understanding of deformation mechanisms preceding macroscopic failure by enabling quantification of the evolving four-dimensional pore network and strain field. Postfailure scanning electron microscopy (SEM) provided supplementary information concerning deformation and failure mechanisms.

In the present study, we illustrate the potential of this emergent experimental technique that can provide data with unprecedented spatial resolution, that is complementary to other experimental techniques such as acoustic emission analysis, and that can contribute to better understanding of deformation processes in rocks. Because this technique enables imaging of both aseismic and seismic deformation and damage in the sample with unprecedented spatial resolution, questions that existing experimental techniques can hardly address may be answered. These include: What is the proportion and spatial distribution of shear relative to volumetric strain events inside the rock prior to failure? What is the proportion of microfracture opening relative to pore opening during dilation? How does the rate of aseismic and seismic damage accumulation evolve as failure is approached?

2. Background

2.1. Failure of Intact Rocks

In rock deformation experiments, the evolution of a specimen is usually characterized while either a constant strain rate or increasing stress is imposed at the boundaries. In true triaxial compression tests, all three principal global strains or stresses, $\sigma_1 > \sigma_2 > \sigma_3$, are controlled. In the experiments reported here, $\sigma_1 > \sigma_2 = \sigma_3 = P_c$, where P_c is the confining pressure, and the maximum principal stress, σ_1, was increased from an initial value of $\sigma_1 = P_c$ at constant P_c, until the sample failed. The sign convention that compressive stress is positive and compressive strain (shortening or a decrease in volume) is positive, which is most commonly used in rock physics, is adopted in this article.

Previous experiments indicate that, for confining pressures on the order of 10 MPa, tensile microcracks nucleate and then undergo dilation, propagation, and coalescence as the differential stress increases, and thereby promote macroscopic failure (e.g., Peng and Johnson 1972; Tapponnier and Brace 1976; Paterson and Wong 2005). Early experiments suggested that dilating microfractures produce macroscopic dilation of rock samples preceding failure (Brace et al. 1966),

and that a critical density of microfractures develops preceding macroscopic shear failure (Scholz 1968; Lockner et al. 1991). The spatial distribution of acoustic emissions indicates that microfractures initially nucleate and grow at apparently random locations in Westerly granite (Lockner et al. 1991). Reches and Lockner (1994) proposed that, as a granite approaches failure, microfractures form elongated arrays inclined at an angle of about 30° relative to the direction of the maximum principal stress until they coalesce into a macroscopic fault. Using high-resolution two-dimensional image correlation analysis, Tal et al. (2016) observed that both local compaction and local dilation occur before failure in a Carrara marble. Experiments on crystalline rocks such as granite, experiments on other brittle materials with preexisting fractures [e.g., poly(methyl methacrylate)], and numerical models suggest that macroscopic dilation occurs through the development of microfractures that are dominated by tensile wing cracks (Horii and Nemat-Nasser 1986; Ashby and Sammis 1990; Kemeny and Cook 1991). Laboratory experiments on analogous rock material that contains frictional flaws suggest that preexisting microfractures coalesce through the propagation and linkage of such tensile wing cracks and secondary shear fractures (e.g., Wong et al. 2001; Dresen and Guéguen 2004). Experiments have also documented how the geometries of preexisting fractures control the coalescence pattern of the resulting wing cracks and shear fractures (e.g., Wong and Einstein 2009). Discrete element method models (Hazzard et al. 2000) and analytical and numerical damage models (Ashby and Sammis 1990; Lyakhovsky et al. 1997; Girard et al. 2010) have produced macroscopic fracture propagation via tensile crack development and long-range elastic interactions.

Analysis of time-lapse three-dimensional X-ray tomograms acquired during deformation of a quartz monzonite rock specimen indicate that the total volume of microfractures, the rate of damage accumulation, and the size of the largest microfracture all increase as power laws and diverge with increasing differential stress as failure is approached (Renard et al. 2018). This behavior suggests that fracture growth within low-porosity crystalline rocks such as monzonite evolves as a critical phenomenon in which

an acceleration of damage accumulation precedes system-size failure, confirming models developed in statistical physics (Dahmen et al. 2009; Girard et al. 2010). In these experiments, most of the fractures formed within grains (i.e., by transgranular fracturing), likely because the rock had low initial porosity (< 1%).

2.2. Micromechanical Models of Sandstone Deformation

Several experimental and analytical studies have characterized the micromechanisms of deformation in sandstones. With increasing effective stresses, the deformation of sandstones transitions from brittle faulting to cataclastic processes (i.e., grain comminution) (Handin et al. 1963; Wong et al. 1997). Depending on the initial rock porosity, in the brittle regime, dilation or shear-enhanced compaction may initiate near a yield point, defined as the point at which a significant deviation from linear elastic behavior occurs (point C′ defined in Brace et al. 1966). At higher effective confining pressures (between $\sim$ 100 and 200 MPa), failure occurs through grain crushing and pore collapse facilitated by microscopic fractures (Wong et al. 1997). At high temperature (900 °C), the failure envelope may transition from a dilatant Mohr–Coulomb relationship to a failure envelope with an elliptical shape as the confining stress increases (e.g., Kanaya and Hirth, 2018).

For sandstones with porosities above $\sim$ 13%, deformation may be dominated by three different mechanisms: shear localization, compaction localization, or cataclastic deformation. Compaction may dominate strain localization, depending on the loading path (e.g., Fortin et al. 2009). Localized compaction bands may be formed in sandstones under high confining pressure conditions (Fortin et al. 2009); For example, at an effective confining pressure of 10 MPa, strain softening and brittle failure occurred in Bleurswiller sandstone specimens with porosities of 23.5–25.3% as the differential stress increased (Baud et al. 2015). At larger effective confining pressures (30–50 MPa), shear-enhanced compaction and shear bands oriented at $\sim$ 30° to the maximum principal stress promoted macroscopic

failure, and at even higher effective confining pressures (70–90 MPa), compaction bands developed (Baud et al. 2015). At the grain scale, fractures within grains and along grain contacts, as well as the collapse of high-porosity volumes, produced the deformation bands.

Menéndez et al. (1996) conducted a series of experiments on Berea sandstone with 21% porosity at constant pore pressure of 10 MPa and confining pressures of 20, 50, and 260 MPa, and characterized postfailure damage in thin sections prepared after failure. At low confining stresses (< 50 MPa), the breakage of grain contacts produced the majority of the damage, and few microfractures propagated through grains. As failure approached, pore collapse and transgranular fractures provided a greater contribution to the overall damage. Tensile fracture along grain contacts dominated the fracture of quartz grains, and shear localization occurred through the coalescence of groups of microfractures. The few observed transgranular fractures led to the conclusion that the development of tensile wing cracks did not play a significant role during the initiation of failure (Menéndez et al. 1996).

During the deformation of a Gosford sandstone with grain size in the range of 0.1–1 mm and 13% porosity, an acceleration of acoustic emissions as failure was approached was measured, as well as a power-law distribution of acoustic emission sizes (Cox and Meredith 1993). A relationship between these acoustic emission parameters and crack dimensions was developed to reconstruct the strain–stress curve and the weakening of the rock as failure was approached.

Zhang et al. (1990) developed a model for the micromechanics of grain crushing under hydrostatic conditions based on the Hertzian contact concept. This model describes the failure of porous rocks using the maximum tangential tensile stress at the edge of the contact area between spherical grains, and linear elastic fracture mechanics assuming a high density of microscopic crack-like flaws with a characteristic length at the grain surfaces (Johnson 1982). This model successfully described the failure envelopes of several sandstones (Baud et al. 2000).

2.3. Deformation of Fontainebleau Sandstone

The relatively homogeneous mineralogy and microstructure of Fontainebleau sandstone at scales greater than the grain size make it an ideal target for deformation experiments. These properties also make this sandstone an ideal candidate for three-dimensional X-ray microtomography imaging studies, and so it was one of the first rocks imaged using this technique (e.g., Auzerais et al. 1996; Coker et al. 1996). Separation of the rock matrix from the pore structure and fracture network by segmentation enabled the first quantitative analysis of the topological and geometrical properties of the pore structure of a sandstone (Lindquist et al. 2000), and led to important insights into the distribution of multiphase fluids in the pore space, and modeling of flow and permeability (Auzerais et al. 1996). These analyses initiated the new field of digital rock physics (e.g., Andrä et al. 2013 and references therein).

Previous studies have analyzed how elastic properties and damage of this rock evolve during deformation (El Bied et al. 2002; Schubnel et al. 2007; Nasseri et al. 2014; Ghaffari et al. 2014; Goodfellow et al. 2015). During triaxial deformation of a 14% porosity Fontainebleau sandstone, Schubnel et al. (2007) recorded series of acoustic emission events preceding macroscopic failure by attaching sensors directly to the rock sample. These recorded precursory events reflect the acoustic energy released by nucleating and propagating microfractures. The acoustic emissions highlighted distinct failure stages: (1) clustered acoustic emissions and strain localization along an incipient fault plane, (2) lack of acoustic emissions within an aseismic nucleation zone, (3) unstable rupture propagation within the previously aseismic, and perhaps locked, zone, and (4) triggering of multiple sets of aftershocks, with the second set of aftershocks emitted from the rupture plane as the pore pressure rapidly dropped (Schubnel et al. 2007). The increasing number of acoustic emissions prior to failure followed an inverse Omori law with a power-law time dependence with an exponent close to 1 (Schubnel et al. 2007). In another series of experiments using a true triaxial stress apparatus with independent control of the three normal stress magnitudes, the failure of a 4.52%

porosity Fontainebleau sandstone included: (1) initial compaction of the rock via crack closure, (2) macroscopic dilation of the sample due to microfractures that opened perpendicular to the minimum stress direction, and (3) accumulation of microfractures until macroscopic failure occurred (Goodfellow et al. 2015).

In the present study, we used X-ray microtomography and three-dimensional DVC analysis to obtain quantitative information about the evolving microfracture networks and pore structure throughout a series of triaxial compression experiments on three air-saturated Fontainebleau sandstone cores. The X-ray attenuation contrast between air and quartz allowed the evolving pore volumes and open microfractures to be distinguished from the rock matrix, thus enabling investigation of deformation via image segmentation (Videos S1 and S2). Three-dimensional digital volume correlation analysis of tomograms can identify diffuse deformation zones, as well as fractures that do not dilate sufficiently to locally decrease the X-ray attenuation (Videos S3, S4, and S5). The main goal of this work is to analyze evolving porosity, and transgranular and intergranular fractures, using segmentation of dynamic X-ray tomograms and digital volume correlation. The results provide new experimental observations of the micromechanisms of deformation and strain localization in sandstone. The results confirm those obtained in previous studies on Fontainebleau sandstone and other porous sandstones (Handin et al. 1963; Menéndez et al. 1996; Wu et al. 2000; El Bied et al. 2002; Schubnel et al. 2007; Nasseri et al. 2014; Goodfellow et al. 2015), and new information was also obtained.

3. Methods and Material

3.1. X-Ray-Transparent Triaxial Deformation Apparatus

The samples were deformed in the X-ray-transparent HADES triaxial apparatus (Renard et al. 2016, 2017), installed on the X-ray microtomography beamline ID19 at the European Synchrotron Radiation Facility. This apparatus enables time-lapse imaging of the sample during compressive

deformation. With the full white beam of the beamline with X-ray energies up to 200 keV, the average energy of X-rays that cross the sample is close to 120 keV after the attenuation of X-rays by the wall of the triaxial rig. Acquisition of a three-dimensional dataset of two-dimensional radiographs required about 1.5 min. The experiments were performed at room temperature (24 °C) on dry cylindrical specimens of 10 mm in length and 5 mm in diameter, corresponding to ~ 50 grains in the axial direction and ~ 20 grains in the radial direction. The voxel size was 6.5 μm. The table in Fig. 1 describes the imposed loading conditions used in these experiments.

The specimens were installed in the rig between two stainless-steel pistons. The lower piston was immobile, and the axial load was imposed on the specimen by displacement of the upper piston. The interfaces between the rock sample and the pistons were not lubricated. Two independent pumps controlled the axial load and confining pressure. In most

laboratory experiments on the deformation and failure of rocks, a constant strain rate is imposed as principal stresses and other quantities of interest, such as acoustic emissions, are measured. This approach cannot be used with X-ray tomography because the resulting tomogram would capture average density contrast data as the specimen deforms over the data acquisition time interval, or 1.5 min in these experiments. Instead, to capture snapshots of deformation, the stress is increased in small steps and X-ray attenuation data are acquired while the strain or stress is held constant. In principle, the structure of the specimen might change during the acquisition time under constant loading conditions if processes such as creep or subcritical fracture propagation occur. However, in these experiments, we did not find evidence for significant changes in structure during data acquisition, such as blurring of the distinct edges between void space and quartz in the tomograms. For other materials or under different conditions, the mechanical behavior may be different, and unacceptable image blurring could occur.

Three experiments were conducted by increasing the differential stress (the difference between the axial stress, σ_1, and the confining pressure) in steps of 2 or 5 MPa far from failure, and steps of 0.5 or 1 MPa close to failure. A jacket made of Viton® fluoropolymer elastomer encased each rock sample, and silicone oil applied the confining pressure to this jacket. In experiment F1, instability of the confining pressure pump produced undulations in the volumetric strain curve (Fig. 1). In this experiment, the confining pressure was held at 20 MPa until the axial stress reached 199 MPa, which closely approached the maximum permissible axial stress of the HADES rig (200 MPa). Under these loading conditions, the sandstone core had not macroscopically failed, so the differential stress was then increased by reducing the confining pressure in steps of 1 MPa from 20 MPa to 14 MPa, at which failure occurred. In this experiment, failure occurred at a differential stress between 185 MPa and 186 MPa. Experiments F2 and F3 were conducted with a constant confining pressure of 10 MPa, and the samples failed before the axial loading reached the limit of the HADES rig.

After each differential stress increase, three-dimensional X-ray microtomography imaging of the

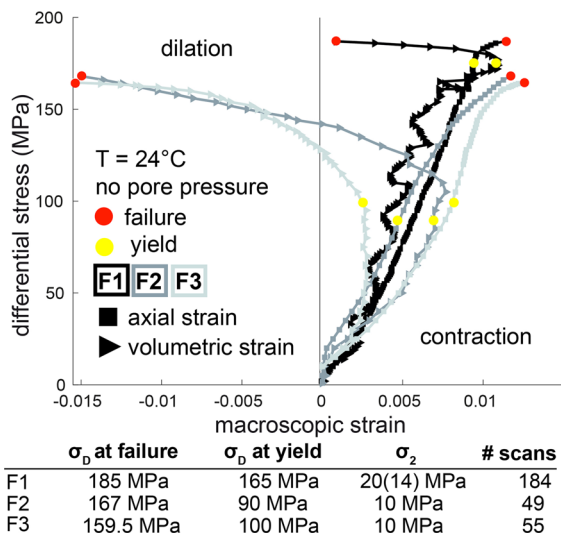|	σ_D at failure	σ_D at yield	σ_2	# scans
F1	185 MPa	165 MPa	20(14) MPa	184
F2	167 MPa	90 MPa	10 MPa	49
F3	159.5 MPa	100 MPa	10 MPa	55

Figure 1

Experimental axial and volumetric strains as functions of the differential stress for the three Fontainebleau sandstone experiments. Each point corresponds to the acquisition of a three-dimensional X-ray tomography dataset. Yellow and red circles show the yield and failure points. The table lists the experimental conditions. In experiment F1, the confining pressure was reduced from 20 MPa after the axial stress reached 199 MPa, and failure occurred when the confining pressure was reduced below 15 MPa at a constant axial stress of 199 MPa (i.e., at a differential stress of 185 MPa). In experiments F2 and F3, the confining pressure was held constant. In experiment F1, the oscillations in the volumetric curve arose from instabilities in the confining pressure pump

specimen was performed. After failure, both the axial stress and confining pressure were decreased, allowing voids to relax and open, and a final imaging step was performed. Each X-ray imaging acquisition required 1.5 min, and each stress increase between scans required 1 min.

Between 49 and 184 datasets, each consisting of 1600 radiographs, were acquired during each deformation experiment, with a total of 288 for the three experiments. From the two-dimensional radiographs, three-dimensional volumes of the specimens ($1600 \times 1600 \times 1600$ voxels) were reconstructed in 16-bit grayscale using a phase-contrast retrieval algorithm (Mirone et al. 2014). During the reconstruction, filters were applied to remove ring artifacts and other spurious patterns, and to correct for the fluctuation of the X-ray source intensity. The grayscale value of each voxel in the three-dimensional volume is proportional to the X-ray attenuation coefficient, itself proportional to local density. Low gray levels (dark shade of gray) correspond to low-attenuating materials (i.e., air), and high gray levels (light shades of gray) correspond to highly attenuating materials (i.e., quartz), while intermediate gray levels correspond to voxels that contain both air and solid (i.e., voxels that are intersected by void boundaries).

In experiments with strain rate loading conditions, the differential stress typically reaches a maximum and then decreases if the confining pressure is not too large. Under stress loading conditions, similar to those used in our experiments, macroscopic failure typically occurs within one stress increment step in brittle rocks. Failure is associated with a macroscopic stress drop. In our experiments, macroscopic failure pulverized the sandstones, producing sand-like material, as well as discrete core-spanning fractures within one stress increment step, and so strain softening following macroscopic failure could not be investigated. The stress–strain relationship and the micromechanical processes that occur prior to failure do not strongly depend on whether the imposed loading are strains or stresses on the time scales of our experiments. Furthermore, our stress loading conditions provided a rich dataset of coalescing fractures prior to macroscopic failure.

3.2. Macroscopic Stress and Strain

The three-dimensional tomograms were used to calculate the axial strain, radial strain, and volumetric strain curves prior to failure (Figs. 1, S1). The macroscopic axial strain was calculated from the distance between the two pistons visible in the tomograms at two locations in an axial plane perpendicular to the piston faces. The average value of these two distances was taken as the height of the sample. The macroscopic radial strain (Fig. S1, inset) was determined by measuring the lengths of two mutually perpendicular transects within horizontal cross sections that intersected the vertical axis at heights of 1/3, 1/2, and 2/3 of the sample height, providing a total of six measurements of the sample diameter, from which the mean value of radial strain was calculated (Fig. S1b). The volumetric strain was calculated from the average height and average radius of the sample during deformation, assuming a cylindrical shape (Fig. 1).

Because of the friction between the ends of the sandstone specimens, we expected that the sandstone specimens would have a slight barrel-like shape under imposed differential stresses, and this was observed (Fig. 4a). So, the volumetric dilatational strain will be somewhat smaller than the volumetric strain calculated with our method that uses core diameters at least 3 mm from the piston–sandstone interfaces. The resolution (and the error) of this macroscopic strain measurement was $10^{-4} l_0$ for the axial strain and $\sim 3 \times 10^{-4} r_0$ for the axial and radial strains, where l_0 and r_0 are the initial length and radius. Consequently, the resolution for the volumetric strain was $\sim 5 \times 10^{-4} V_0$, where V_0 is the initial volume. The resolution was higher for the axial strain because there was a higher X-ray attenuation contrast between the pistons and the sample, which controlled the axial strain measurement, than between the jacket and the sample, which controlled the radial strain measurement.

3.3. Segmentation Procedure and Microscopy Imaging

To determine the pore and fracture sizes and shapes from the tomograms (Fig. 2b), the following
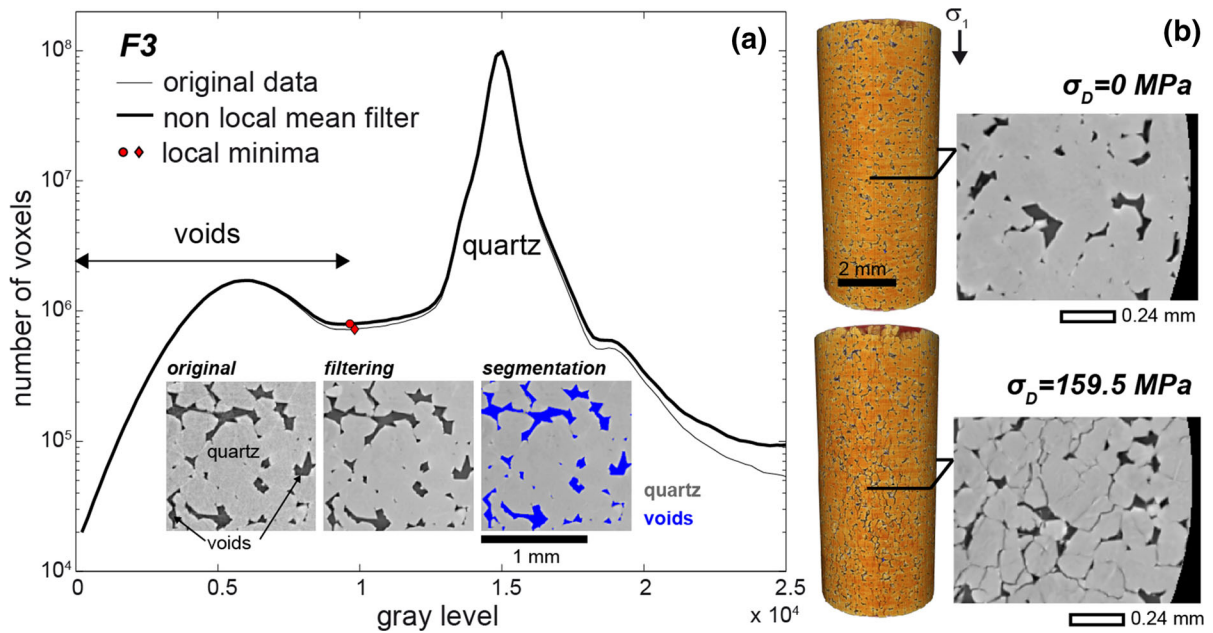
Figure 2
Thresholding procedure used to segment the three-dimensional datasets into quartz matrix and air-filled voids, including pores and fractures. **a** Distribution of the gray levels of experiment F3 for the original three-dimensional dataset (thin line) at a differential stress of 10 MPa, before and after applying the nonlocal mean filter (thick line). Insets show two-dimensional slices of the sample with the unfiltered data (left), filtered data (middle), and segmented data (right). We selected the local minima of the histogram between the peaks arising from voids (left peak) and from quartz grains (right peak) to segment the tomograms into quartz grains and voids. The red symbols show the minima of the original (diamond) and filtered (circle) data, which do not differ significantly. **b** Three-dimensional rendered view of the specimen before and after experiment, and two-dimensional horizontal cross-sections. Video S2 shows the time-lapse evolution of the specimen in this experiment

procedure was applied using the software Avi-zoFire®: (1) denoising of the three-dimensional volumes with a nonlocal mean filter (Buades et al. 2005), (2) application of a mask to remove the jacket, pistons, and confining oil around the rock sample, (3) application of a nonlocal median filter to sharpen the boundaries between intact rock material and voids (pore space or fractures), and (4) thresholding the data to partition the voxels occupied primarily by air from those occupied primarily by quartz (Fig. 2a).

Representative histograms from a three-dimensional dataset (experiment F3) show how thresholding can differentiate between voids and the rock matrix, which is composed primarily of quartz (Fig. 2). The grayscale values of the tomograms correspond to the X-ray attenuation produced by materials, which is lower for air than for quartz grains. Both the original and filtered histograms show two peaks corresponding to the voids (low X-ray attenuation) and the quartz grains (high X-ray

attenuation). The local minimum in the histogram of the filtered data was used to separate the voids from the grains (red markers in Fig. 2). We also tested segmentation of the data using the midpoint between the two peaks, and the results were similar to those using the minima. We conclude that at least two criteria could be used to select a threshold gray value to separate voids and grains. Here, we chose the minimum value between the two peaks of the histogram to segment the data.

Filtering the tomograms reduced the noise and enhanced the contrast between pores and grains, but it produced only small differences in the histogram and minimum. Thresholding with the histogram minimum enabled extraction of pores and major microfractures from the three-dimensional volumes. For the complete series of tomograms acquired during each experiment, the same threshold value was used to segment the data. However, this thresholding technique did not unambiguously capture

microcracks with apertures less than or approximately equal to the imaging resolution, although they could be identified by inspection of the tomograms by eye.

Some parts of the specimens were recovered in their jackets at the end of experiments F1 and F2 after unmounting them from the HADES rig. For experiment F2, almost the entire specimen could be recovered, but specimen F3 was mostly reduced to quartz particles. The specimens from experiments F1 and F2 were impregnated with liquid epoxy resin and then cut along the axial plane after the liquid epoxy had formed a cross-linked polymeric solid. The exposed surface was polished, coated with 10 nm gold, and imaged using a Hitachi SU5000 scanning electron microscope at the University of Oslo with a voltage of 15 kV.

3.4. Digital Volume Correlation Analysis

Three-dimensional digital volume correlation (DVC) analysis was initially developed for applications in mechanics and engineering (e.g., Bay et al. 1999 and references therein). DVC analysis finds the translations and rotations that best map subvolumes within a three-dimensional dataset onto subvolumes in another three-dimensional dataset by identifying similar patterns within those subvolumes. This technique has been used to study the development of shear bands in soils (Viggiani et al. 2004), and the compaction of a Rothbach sandstone specimen with a strain resolution of 10^{-3} (Louis et al. 2007). We used the open-source DVC analysis software TomoWarp2 for our DVC analyses (Hall et al. 2010; Tudisco et al. 2015, 2017).

DVC analysis is based on finding the displacement field that maximizes the correlation between voxel intensity subsets (subvolumes) within pairs of sequential tomograms. Interpolation methods enable subvoxel-scale displacement resolution to be obtained. However, if there is little variation in X-ray attenuation coefficients within the subvolumes, DVC analysis may lead to unreliable incremental displacement fields; For example, there is little or no variation in the X-ray attenuation coefficients within individual quartz grains, except perhaps lower-density fluid inclusions. Consequently, the parameters of DVC analyses must be tuned to capture displacement fields that include subvolumes that include several grains or grain boundaries, or other contrasts in the X-ray attenuation coefficient fields.

By identifying similar patterns across successive volumes, digital volume correlation produces three-dimensional displacement fields from which the six independent components of the second-rank three-dimensional strain tensor may be calculated. These incremental strain fields reveal strain localization that occurred within the time interval between the acquisitions of the pair of microtomograms. The cumulative strain from the onset of loading could also be determined. Following the approach of McBeck et al. (2018), we calculated three-dimensional incremental displacement fields between pairs of three-dimensional tomograms corresponding to approximately constant increments in the macroscopic axial strain, ε_{zz}^{M}, throughout each experiment. We calculated ε_{zz}^{M} from the change in axial length of the sandstone specimen relative to the initial length l_0, as described in Sect. 3.2. In addition, to investigate in more minute detail the dominant failure modes near the onset of yielding in experiment F2, we used DVC analysis to calculate the incremental strain fields surrounding the yield point, with the highest possible temporal (i.e., differential stress) resolution.

We calculate changes in the local volumetric and shear strain fields using the first invariant of the incremental strain tensor, $I_1(\Delta\varepsilon) = \varepsilon_{xx} + \varepsilon_{yy} + \varepsilon_{zz}$, and the second invariant of the incremental strain tensor, $I_2(\Delta\varepsilon) = (\varepsilon_{xy})^2 + (\varepsilon_{xz})^2 + (\varepsilon_{yz})^2 - (\varepsilon_{xx}\varepsilon_{yy} + \varepsilon_{xx}\varepsilon_{zz} + \varepsilon_{yy}\varepsilon_{zz})$, where ε_{ij} is a component of the local incremental strain tensor, i.e., the local strain calculated by comparing two successive tomograms in the DVC analysis. In this coordinate system, the z axis is vertical (parallel to σ_1) and the x–y plane is horizontal (perpendicular to σ_1). $I_1(\Delta\varepsilon)$ provides information about the volumetric strain in coordinate systems independent of the principal axis system. To characterize the incremental shear strain, we calculated the second invariant of the incremental deviatoric strain, $J_2(\Delta\varepsilon)$. Since $(3J_2(\varepsilon))^{\frac{1}{2}}$ is the von Mises yield criterion equivalent strain, we refer to $(3J_2(\Delta\varepsilon))^{\frac{1}{2}}$ as the von Mises incremental strain. The second invariant of the incremental deviatoric strain, $J_2(\Delta\varepsilon)$, is related to the first invariant $I_2(\Delta\varepsilon)$, and the second
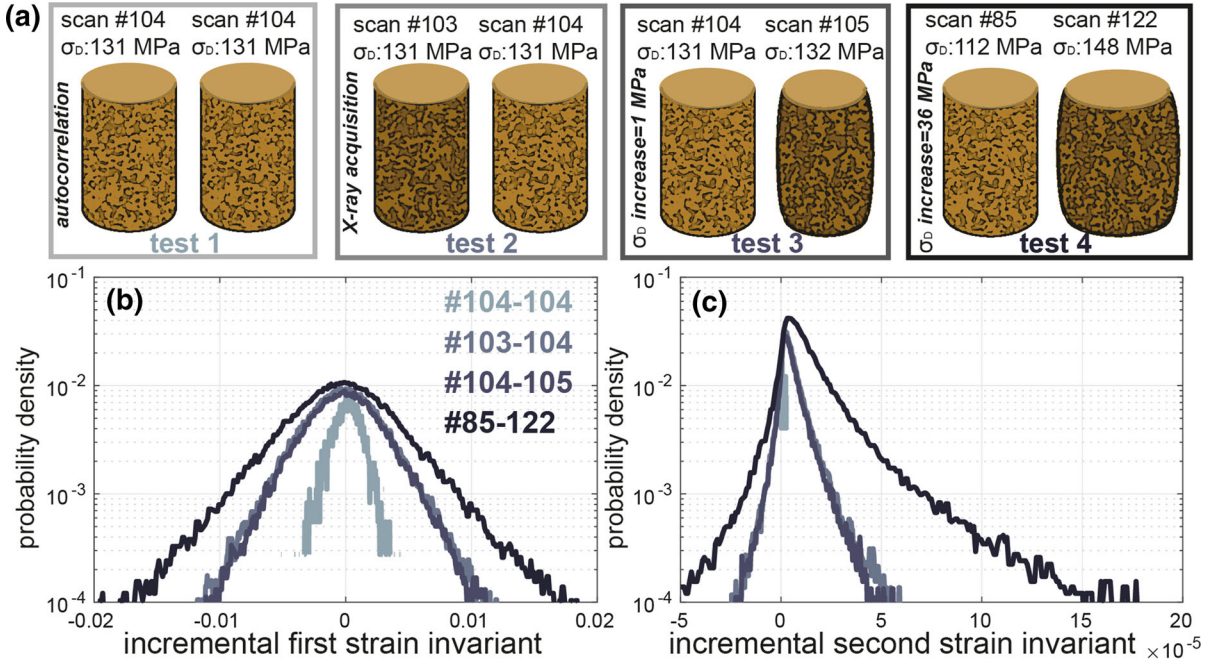
Figure 3
Characterization of the resolution of the digital volume correlation technique using four tests. **a** Pairs of three-dimensional datasets used in the four tests of digital volume correlation analysis. **b**, **c** Results of the tests. The gray level of the boxes surrounding each pair of tomograms in (**a**) matches the gray levels of the probability densities shown in (**b**) and (**c**). The strain resolution is taken as twice the standard deviation found in test 2 between scans #103–104, a more conservative estimate of the error than test 1

invariant, $I_2(\Delta\varepsilon)$, of the incremental strain tensor by $J_2(\Delta\varepsilon) = \frac{1}{3}(I_1(\Delta\varepsilon))^2 - I_2(\Delta\varepsilon)$. To be able to compare the values of $I_1(\Delta\varepsilon)$ (first order in the strain) and $J_2(\Delta\varepsilon)$ (second order in the strain), we report in the following the values of $(3J_2(\Delta\varepsilon))^{1/2}$. In the adopted sign convention, negative values of $I_1(\Delta\varepsilon)$ indicate volumetric dilation, and positive values of $I_1(\Delta\varepsilon)$ indicate volumetric contraction.

The windows used to perform the DVC correlations had a cubic shape with four faces parallel to the main compressive stress σ_1 and two faces perpendicular to it. Following tests on the influence of the correlation window size and node spacing size on the resolution, computation time, and robustness of the resulting displacement fields, we selected a correlation window size of 10 voxels (65 μm) and node spacing size of 20 voxels (130 μm). This choice ensured that each window contained at least a subvolume of one grain and a subvolume of one pore, maximizing the contrast for volume correlation. To characterize the resolution of strain values

obtained from DVC analysis in these experiments, and thus the lower limit of robust strain values, we performed DVC analysis on: (1) the same tomogram (i.e., autocorrelation), (2) two tomograms that were acquired at the same differential stress, (3) two tomograms that were separated by 1 MPa of differential stress (131 MPa and 132 MPa), and (4) two tomograms that were separated by 36 MPa of differential stress (112 MPa and 148 MPa) (Fig. 3a).

The resulting strain populations show that the autocorrelation (test 1) produced smaller strain magnitudes than the other tests, as expected (Fig. 3b, c). The nonzero displacement field produced in this autocorrelation calculation arises from interpolation between integer (pixel) displacements in the subpixel resolution method used in the TomoWarp2 software. The strain populations of test 2 and test 3 were similar to each other, indicating that a differential stress increase of 1 MPa did not produce significant deformation of the sandstone in this increment of the experiment. The larger strain magnitudes produced in

test 4 indicate that, as expected, more strain accumulated during the 36 MPa of differential stress increase than during the 1 MPa of differential stress increase of test 3.

The incremental strain populations produced in the autocorrelation test (test 1) suggest a characteristic error in the calculated strains (Fig. 3b, c). Twice the standard deviation of the $I_1(\Delta\varepsilon)$ and $I_2(\Delta\varepsilon)$ populations produced in test 2 were used as the thresholds for the populations of these two invariants. These thresholds are more conservative than those produced in the autocorrelation of test 1, and so produce strain populations with lower ratios of signal to noise. Invariants with magnitudes below these thresholds, which are on the order of 10^{-3} for $I_1(\Delta\varepsilon)$ and $I_2(\Delta\varepsilon)$, were removed from the incremental strain fields.

3.5. Fontainebleau Sandstone Samples

Fontainebleau sandstone is a quartz arenite of Oligocene age outcropping around Fontainebleau City near Paris, France (Bourbie and Zinszner 1985). This sandstone is considered an ideal reservoir rock because it has a relatively homogeneous mineralogical composition (> 99% quartz), well-sorted grain size with an average diameter of 0.25 mm, and a wide range of porosities (3–30%) depending on the degree of quartz cementation. As expected for a clean sandstone with a characteristic grain diameter of 0.25 mm, the high-porosity specimens have a high permeability (Bourbie and Zinszner 1985). In specimens with porosities higher than 5%, most of the pores are connected in three dimensions (Fredrich et al. 1993). For samples with porosities smaller than 4%, the pore space is less connected, so the permeability is at least one order of magnitude lower than that of samples with higher porosities (Fredrich et al. 1993). In addition, the P-wave velocity in this sandstone decreases almost linearly from 5500 to 3000 m s^{-1} as the porosity increases from 3 to 30% (Bourbie and Zinszner 1985).

In the present study, three specimens of diameter 5 mm and length 10 mm were cored perpendicular to bedding from a single $10 \times 10 \times 10$ cm^3 Fontainebleau sandstone block with a matrix made of quartz and a minor amount (< 1%) of iron oxides.

The mean grain size was 0.25 mm. The porosity derived from the initial three-dimensional datasets following segmentation was in the range of 5.5–7%. The porosity was also measured by weighing ten dry specimens before and after imbibition with water, and a value of $6 \pm 1\%$ (standard deviation) was obtained, consistent with the porosity measured using X-ray tomography. Three-dimensional imaging indicates that the initial pore structure was almost entirely connected in three dimensions. There was almost no microporosity in these specimens (i.e., porosity within grains), except for a few micrometer-size fluid inclusions in the quartz grains that were not connected to the bulk porosity.

4. Results

4.1. Macroscopic and Microscopic Deformation

In each experiment, the macroscopic axial strain increased faster than a linear trend (i.e., superlinearly) relative to the applied stress until the differential stress reached about 20 MPa. This initial nonlinear phase arose from the closure of the weakest preexisting microfractures and pores, grain reorientation, and the deformation of weak intergrain contacts. In experiments on Mount Scott granite, Katz and Reches (2004) observed inconsistencies in the initial, low differential stress behavior (an increase in the deformation modulus, $\partial\sigma_D/\partial\varepsilon_M|_{P_c}$) with increasing strain for some specimens and a decrease in the deformation modulus for others. Consequently, we cannot conclude that the initial softening ($\partial^2\sigma_D/\partial\varepsilon_M^2|_{P_c} < 0$) is generic for low-porosity Fontainebleau sandstone under a confining stress of 10 MPa. In addition, the closure of microfractures and pores may cause hardening rather than softening. However, the initial softening was more pronounced in our experiments than those of Katz and Reches (2004). We did not investigate these initial mechanisms in detail because the focus of this work was on the damage preceding macroscopic failure.

After the initial nonlinear phase, the macroscopic mechanical behavior transitioned gradually from a quasilinear phase at intermediate differential stresses (20–80 MPa), to significant deviation from

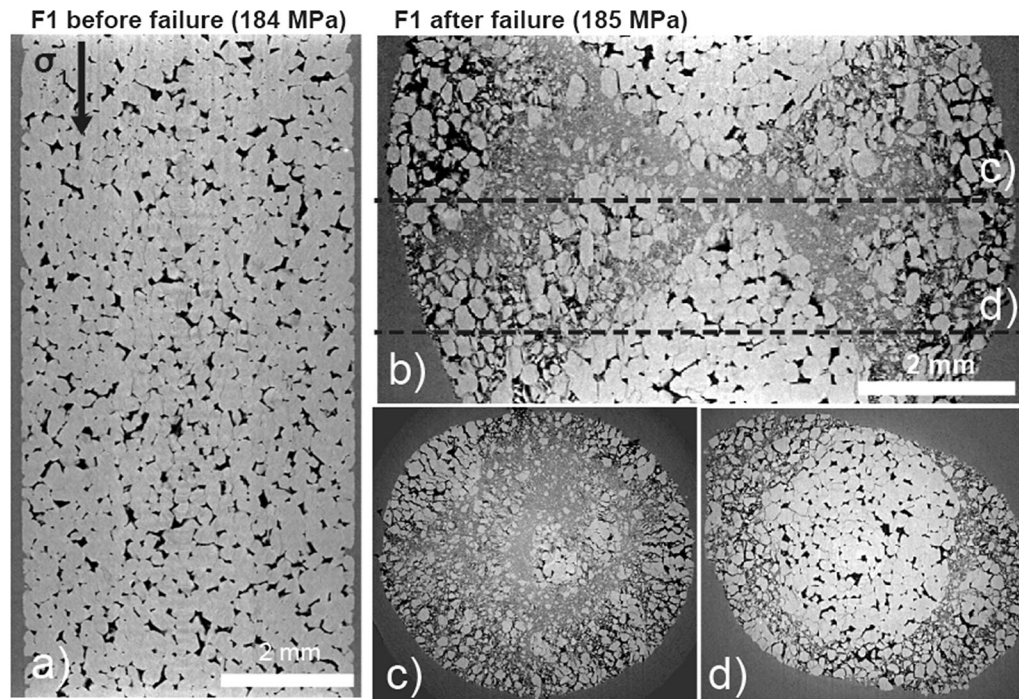**F1 before failure (184 MPa)   F1 after failure (185 MPa)**

Figure 4
Two-dimensional views of experiment F1 immediately preceding and following macroscopic failure at differential stresses of 184 and 185 MPa. **a** Vertical axial transect at the onset of failure showing quartz grains, pores, and microfractures oriented subparallel to the main compressive stress direction (vertical). **b** Vertical transect of the sample after macroscopic failure. Compared with **a**, the sample has shortened and widened significantly because of failure. Dashed lines indicate the location of the two perpendicular (horizontal) cross sections shown in **c** and **d**. The sample failed through the formation of conical fracture zones in which grains were comminuted

quasilinear behavior associated with significant dilation, and finally to macroscopic failure (Fig. 1). We chose to define the yield point as the point at which the measured volumetric strain differed by 3% from the strain predicted by linear regression of the mean stress–strain data over the range $20 \leq \sigma_D \leq 80$ MPa (also named point C′ in Brace et al. 1966). After the yield point was reached, the relationship between the differential stress and axial strain became increasingly nonlinear until macroscopic failure occurred. The yield point corresponded to an axial strain close to 0.08 for experiments F1 and F3 and to 0.04 for experiment F2 where a fault localized near the yield point. The volumetric strain curves revealed that the sample compacted (volumetric strain increased) preceding the yield point, and then began to dilate (volumetric strain decreased) near the yield point in each experiment (Fig. 1). Following yielding and preceding macroscopic failure, microfractures propagated through grains as well as along grain

boundaries (Figs. 2b, 4a, 5a–c, 6c, 7, Videos S1 and S2).

Consistent with the similar stress–strain curves of experiments F1 and F3, the evolving microfracture distributions were also similar in these experiments. In particular, damage remained diffuse and distributed throughout much of each experiment (Fig. 4a), and only concentrated into a narrower zone close to failure ($\sim$ 95% of the failure stress) (Video S2). In contrast, in experiment F2, damage localized early ($\sim$ 75% of the failure stress) along a narrow planar zone that evolved into a fault (Fig. 5, Video S1). These differing behaviors are also revealed in the spatial distribution of high strains from the DVC analyses. The incremental strains above the 95th percentile of each strain population were more spatially diffuse in experiments F1 (Video S3) and F3 (Video S5) than in experiment F2 (Video S4). Despite these differences in strain localization preceding failure, the development of conical faults, in
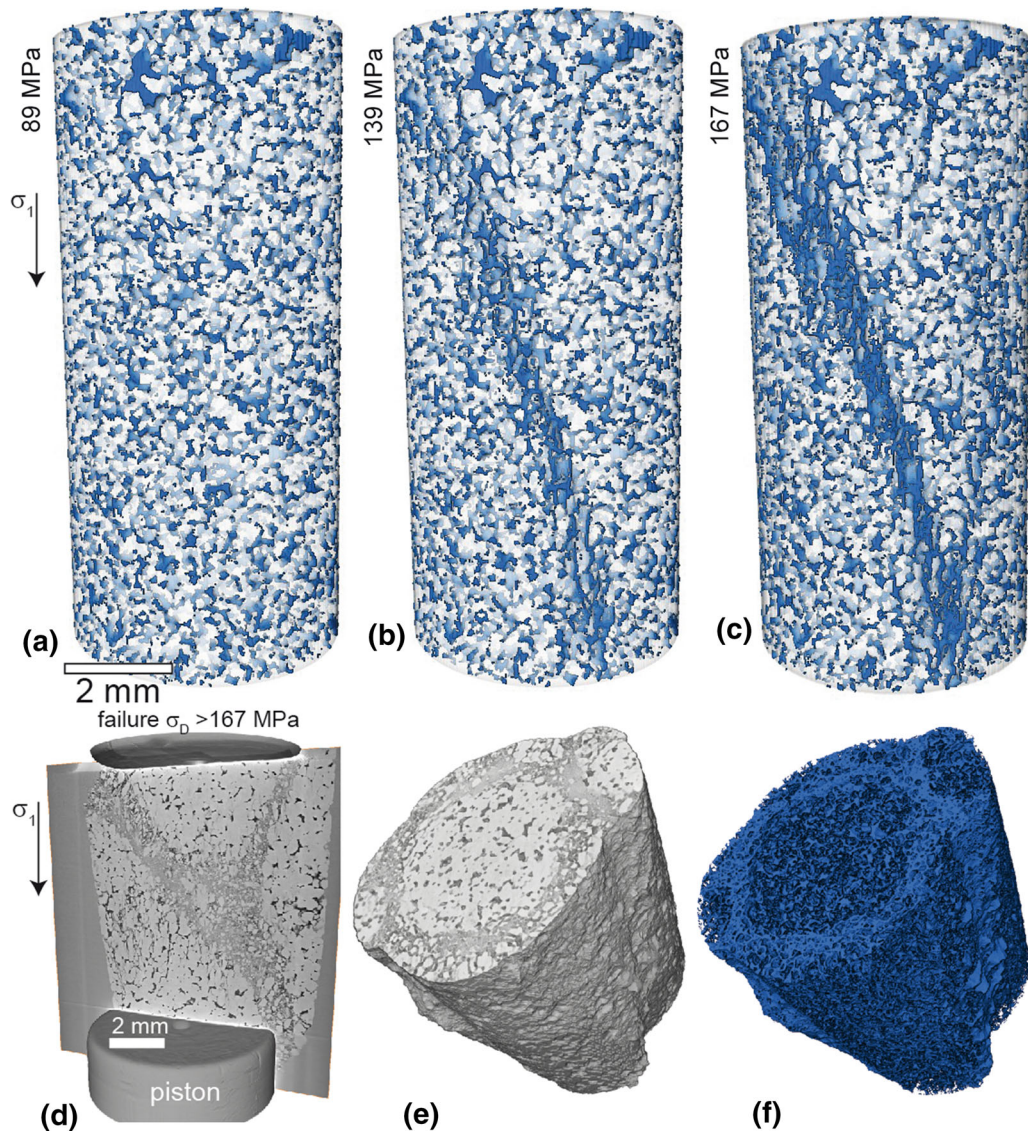
Figure 5
Evolution of pore space and fracture networks in experiment F2. **a–c** Three-dimensional rendered views of the specimen at increasing differential stresses. Porosity and fractures are shown in blue, and the quartz matrix is shown in white. **c** The onset of failure (167 MPa). Video S1 shows a complete time-lapse three-dimensional rendered view of the specimen throughout the experiment. **d** Sample after failure ($\sigma_D > 167$ MPa) with the two pistons of the HADES rig displayed. **e** Three-dimensional rendered view of the sample after failure with comminuted grains. **f** Structure of the porous network, which was 99% connected in three dimensions both preceding and following failure. Following failure, the porosity in the fracture zones that host comminuted grains was smaller than the porosity in the other parts of the rock, where the pore space is similar to that in the rock before loading

which grain comminution and porosity reduction occurred, ultimately caused the macroscopic failure of each sandstone sample (Figs. 4b–d, 5d–f). Dilatational shear failure was the main mechanism of faulting, and significant compaction, grain comminution, and porosity reduction were observed in the final

fault zone. The fractures developed into conical shapes because the pistons of the rig were not lubricated. This lack of lubrication produced frictional resistance to lateral movement of the sandstone in contact with the pistons, which localized shear strain and so promoted fracture nucleation near the
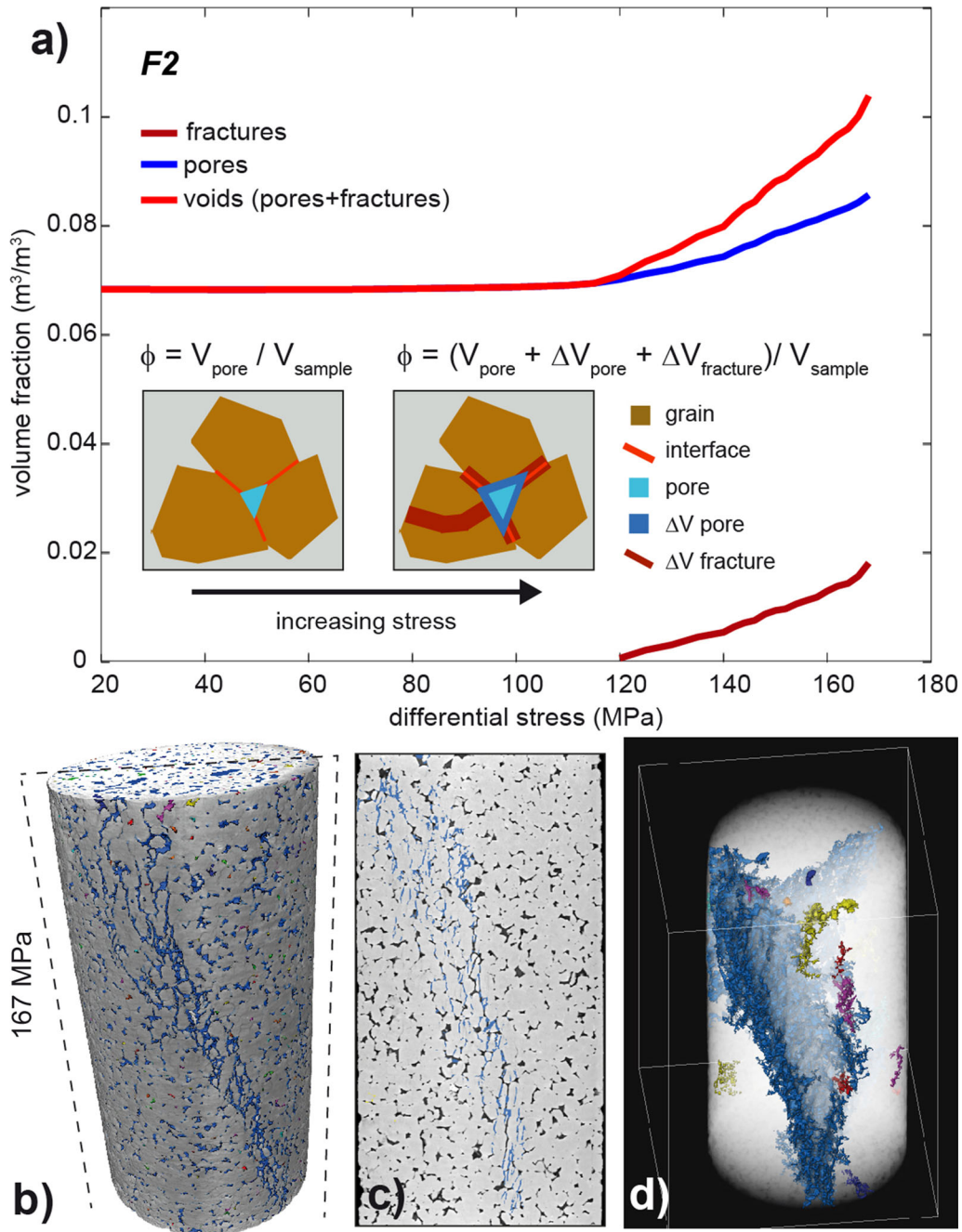
Figure 6
Pores and fractures identified after segmentation of the three-dimensional datasets of experiment F2. **a** Evolution of the pore, fracture, and total void (i.e., pore + fracture) volume fractions as a function of the differential stress. The total void volume fraction (red curve) can be separated into propagating fractures (blue curve) and expanding pores (dark-red curve) in this experiment. The inset sketch shows how the pore and fracture volumes increased. **b–d** Results of segmentation for experiment F2 at a differential stress of 167 MPa. **b** Three-dimensional rendered view of the specimen at the onset of failure with quartz shown in light gray, and pores and fractures shown in colors. **c** Vertical transect of the previous image, with fractures shown in blue, pore space shown in black, and quartz shown in light gray. **d** Three-dimensional view of the microfracture network shown in blue and other colors. Each color shows a unique, unconnected, fracture network

edges of the top and bottom sandstone–piston interfaces (e.g., Peng and Johnson 1972). Consequently, the boundary condition at the pistons may have controlled the final angle of the faults at failure.

In all the experiments, more than 99% of the voids, including the pores and fractures, were connected in three dimensions (Fig. 6b), both preceding and following faulting (Fig. 5). In experiment F2, the gray levels (X-ray attenuation coefficients) of the fractures were slightly higher than those of the pores, enabling segmentation of the fractures from the pore space (Fig. 6). This segmentation revealed that a core-spanning fracture developed through the linkage of subvertical, dilating microcracks (Fig. 6b, c). The core-spanning fracture did not immediately result in macroscopic failure denoted by a reduction in the axial stress. This segmentation also enabled separation of the contributions to the total porosity increase from the growth of preexisting pores, and the propagation and opening of new fractures (Fig. 6a).

Observations of microstructures at the grain scale using scanning electron microscopy (SEM) and visual inspection of the tomograms at the micrometer scale enabled various deformation mechanisms to be differentiated, including intergranular fracturing (i.e., grain boundary opening), transgranular fracturing, and grain comminution (Fig. 7). Each of the sandstone cores failed macroscopically through the development of conjugate faults (Figs. 4b, 5d, 7a). Cracks propagated both within the quartz grains (i.e., transgranular fractures) (Fig. 7b, d) and between grains (i.e., intergranular fractures) (Fig. 7c). In some cases, these cracks stopped at a pore interface. In experiment F2, the cracks self-organized into an incipient fault in which shear displacements could be observed (Fig. 7g–i).

In summary, the three samples have similar macroscopic stress–strain relationships characterized by: (1) initial macroscopic compaction arising from the closing of voids, (2) macroscopic dilation arising from microfracture development and pore opening, (3) transgranular and intergranular propagation of fractures that drives the strain–stress relationship from linear to nonlinear, and (4) macroscopic shear failure due to the coalescence of microscopic fractures. These macroscopic behaviors arose from microscopic deformation processes that the four-

dimensional strain tensors revealed. In experiments F1 and F3, damage localized into a narrow deformation zone near macroscopic failure. In contrast, in experiment F2, damage began to localize into a narrow zone near the macroscopic yield point, and the core-spanning fault grew slowly enough to be captured in several tomograms preceding macroscopic failure.

4.2. Global Evolution of Damage toward Failure

To characterize the evolution of cumulative damage toward failure, we extracted the voids from the quartz grains in each tomogram. Segmentation into rock matrix and voids (pores and fractures) provided the volume fraction of voids as a function of increasing differential stress (Figs. 6, 8, S2). To quantify the accumulation of damage, including opening pores and propagating fractures, Renard et al. (2018) employed a damage index, $D_\phi = \frac{\phi - \phi_i}{1 - \phi_i}$, where ϕ_i is the initial void fraction of the sample under the initial confining pressure, preceding axial loading, and ϕ is the void fraction measured at a given differential stress. In this approach, the normalized distance to failure in stress space is defined as $\Delta = \left(\frac{\sigma_f - \sigma}{\sigma_f} \right)$, where σ_f is the differential stress at which failure occurred, and σ is the differential stress when the tomogram was acquired. When $\Delta = 0$, the rock is at failure, and when $\Delta = 1$, no differential stress is applied to the sample. Renard et al. (2018) applied this normalization to show that damage accelerates as a power law in quartz monzonite ($\partial D_\phi / \partial \sigma \sim \Delta^{-\beta}$), in agreement with mechanical models that consider failure as a critical phenomenon (Dahmen et al. 2009; Girard et al. 2010). This behavior suggests that failure is a critical phenomenon in crystalline rocks such as monzonite.

However, in our sandstone experiments, D_ϕ did not increase as a negative power of Δ as failure was approached. In these experiments, the total porosity, ϕ, and the damage index, D_ϕ, remained near their initial values until the differential stress was several MPa smaller than the differential stress at yield point, and then changed rapidly until failure occurred (Fig. 8a). This acceleration of D_ϕ could not be fitted by a power law or an exponential relationship
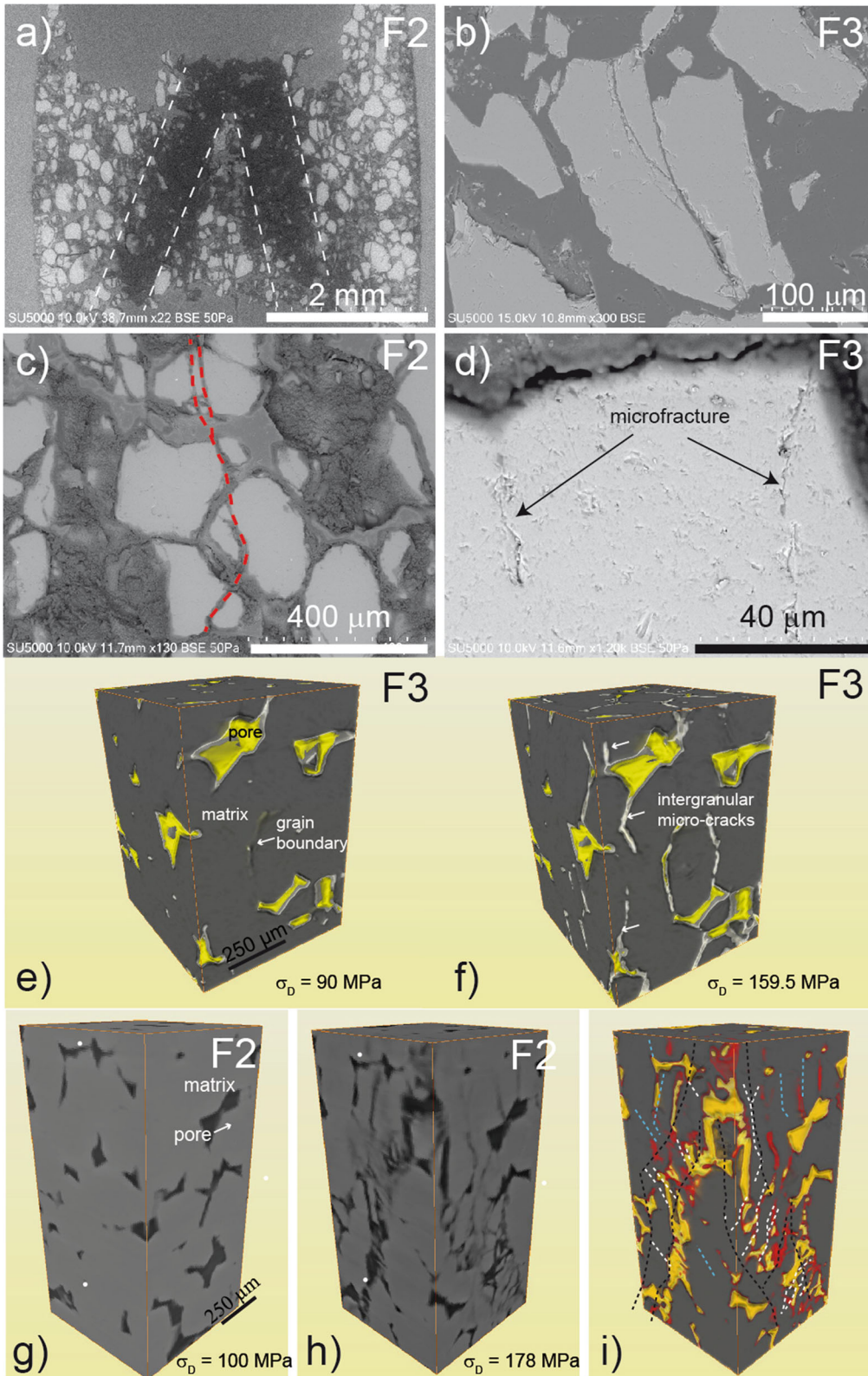
◄Figure 7

Microstructures of deformation. **a–d** Scanning electron microscopy images of samples F2 and F3 after failure. **a** Sample F2 with fault zones highlighted by white dashed lines. **b** Transgranular fracture. **c** Transgranular fractures that may have been produced by a directed force network, or chain (dashed red lines). **d** Onset of microfractures in a quartz grain. **e**, **f** Three-dimensional rendering of X-ray microtomograms from experiment F3 **e** before and **f** after failure showing mostly intergranular fractures. Yellow shows porosity, and white shows intergranular fractures. Three-dimensional rendered views of experiment F2 **g** before and **h**, **i** after failure showing both intergranular and transgranular fractures. **i** Red highlights damaged areas. **g**, **h** White dots show strain markers in both images. **i** White dotted lines highlight shear bands. Blue dotted lines show intergranular and transgranular fractures. Dark dotted lines highlight the fault zones

(Fig. 8b), so this relationship differs from the power-law acceleration observed for the crystalline quartz monzonite (Renard et al. 2018). Due to the instability of the confining pressure pump in experiment F1, we focus on the evolving damage index in experiments F2 and F3 (Fig. 8). Figure S2 shows the results from all three experiments. We interpret the absence of power-law behavior as the pinning of microfractures when they reach pore walls: the presence of pores screens the stress concentration at the fracture tips,

which may reduce the long-range elastic interactions necessary to develop a power-law increase of damage as failure is approached (Dahmen et al. 2009; Girard et al. 2010).

4.3. Evolving Statistics of Incremental Strains

To further characterize the evolution of microscopic damage, we performed DVC analysis of sequential pairs of tomograms in each experiment. The resulting series of three-dimensional incremental strain tensor fields, normalized by division by the incremental macroscopic axial strain, $\Delta\varepsilon_{zz}^{M}$,, enabled quantitative assessment of the evolving volumetric and shear strain localization (Fig. 9). The normalization by $\Delta\varepsilon_{zz}^{M}$ was performed because the macroscopic strain increase between pairs of tomograms was not constant (Fig. 10a, b, g). The top 5% of the negative $\frac{\Delta I_1(\Delta\varepsilon)}{\Delta\varepsilon_{zz}^{M}}$ (dilatational), positive $\frac{\Delta I_1(\Delta\varepsilon)}{\Delta\varepsilon_{zz}^{M}}$ (contractive), and $\frac{(3\Delta J_2(\Delta\varepsilon))^{1/2}}{\Delta\varepsilon_{zz}^{M}}$ (shear) populations in five differential stress increments of each experiment (Fig. 9, Videos S3–5) revealed the localization of the core-spanning fracture observed in experiment F2 (Figs. 5a–c, 6b–d,
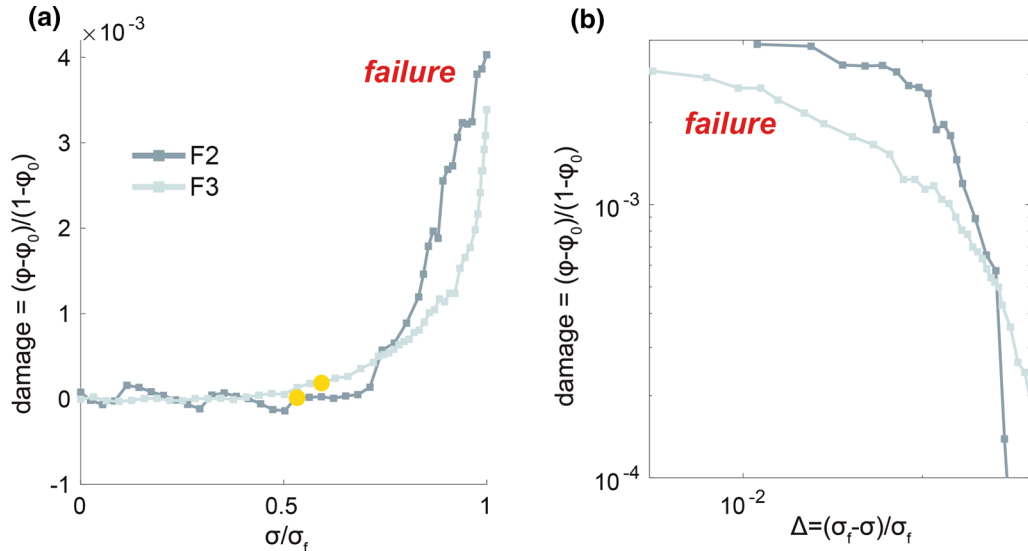

Figure 8

Evolution of the damage index as the sandstone specimens approached failure in experiments F2 and F3. Figure S2 shows data from experiment F1. **a** Evolution of the damage index as a function of the differential stress normalized by the differential stress at failure, σ/σ_f. The porosity and damage index increased as the differential stress approached the differential stress at failure. **b** Evolution of the damage index as a function of the normalized distance to failure, $\Delta = (\sigma_f - \sigma)/\sigma_f$, in log–log space. Failure occurred when $\sigma/\sigma_f = 1$ in **a** and when $\Delta = 0$ in **b**. Yellow circles show the yield points
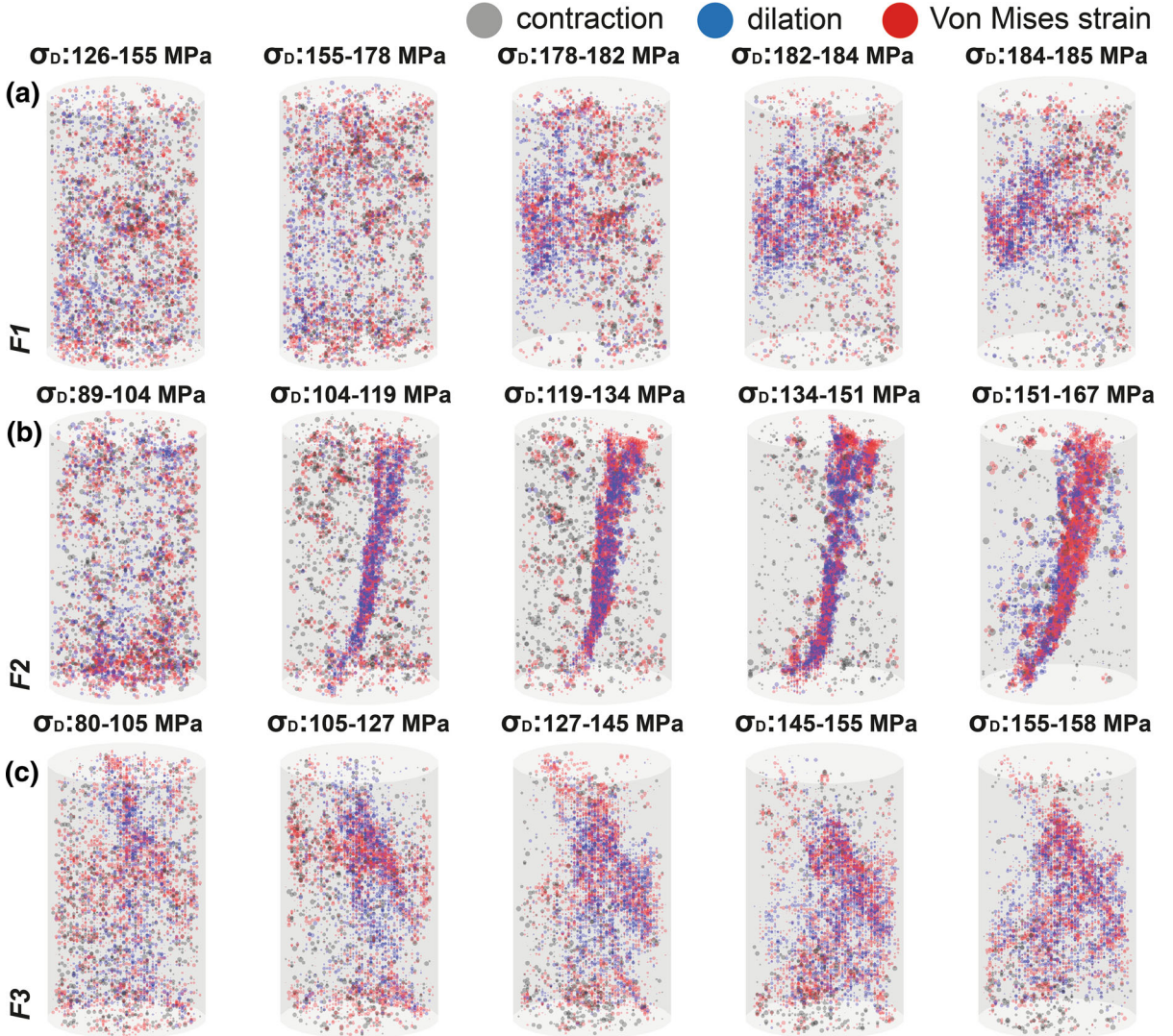
Figure 9

Spatial distribution of incremental strain invariant magnitudes above the 95th percentile of each incremental strain population for experiments F1 (**a**), F2 (**b**), and F3 (**c**). The sizes of the points are proportional to the magnitude of the incremental strain invariants. Gray dots show the contractive $\frac{I_1(\Delta\varepsilon)}{\Delta\varepsilon_{zz}^{M}}$, blue dots show dilatational $\frac{I_1(\Delta\varepsilon)}{\Delta\varepsilon_{zz}^{M}}$, and red dots show the Von Mises incremental strain, $\frac{(3J_2(\Delta\varepsilon))^{1/2}}{\Delta\varepsilon_{zz}^{M}}$, used here to characterize shear strain. The differential stresses above each figure indicate the stresses at which the pairs of tomograms used in the DVC analysis were acquired. Videos S3–S5 show the spatial distribution of high strains throughout each experiment

Video S2). While segmentation of the tomograms provided information about the evolving dilatational, contractional, and shear strain as well as pore volumes, fractures, and their connectivity, DVC analysis provided displacement fields from which strain fields were calculated with a strain resolution close to 10^{-3} for these scans.

We calculated the incremental strain fields between pairs of three-dimensional datasets that were separated by an approximately constant change in the macroscopic axial strain, $\Delta\varepsilon_{zz}^{M}$. For each experiment, ten incremental strain fields that encompassed each complete experiment were calculated (Fig. 10). To track the interplay between nondeviatoric and deviatoric strains, we report histograms of the first
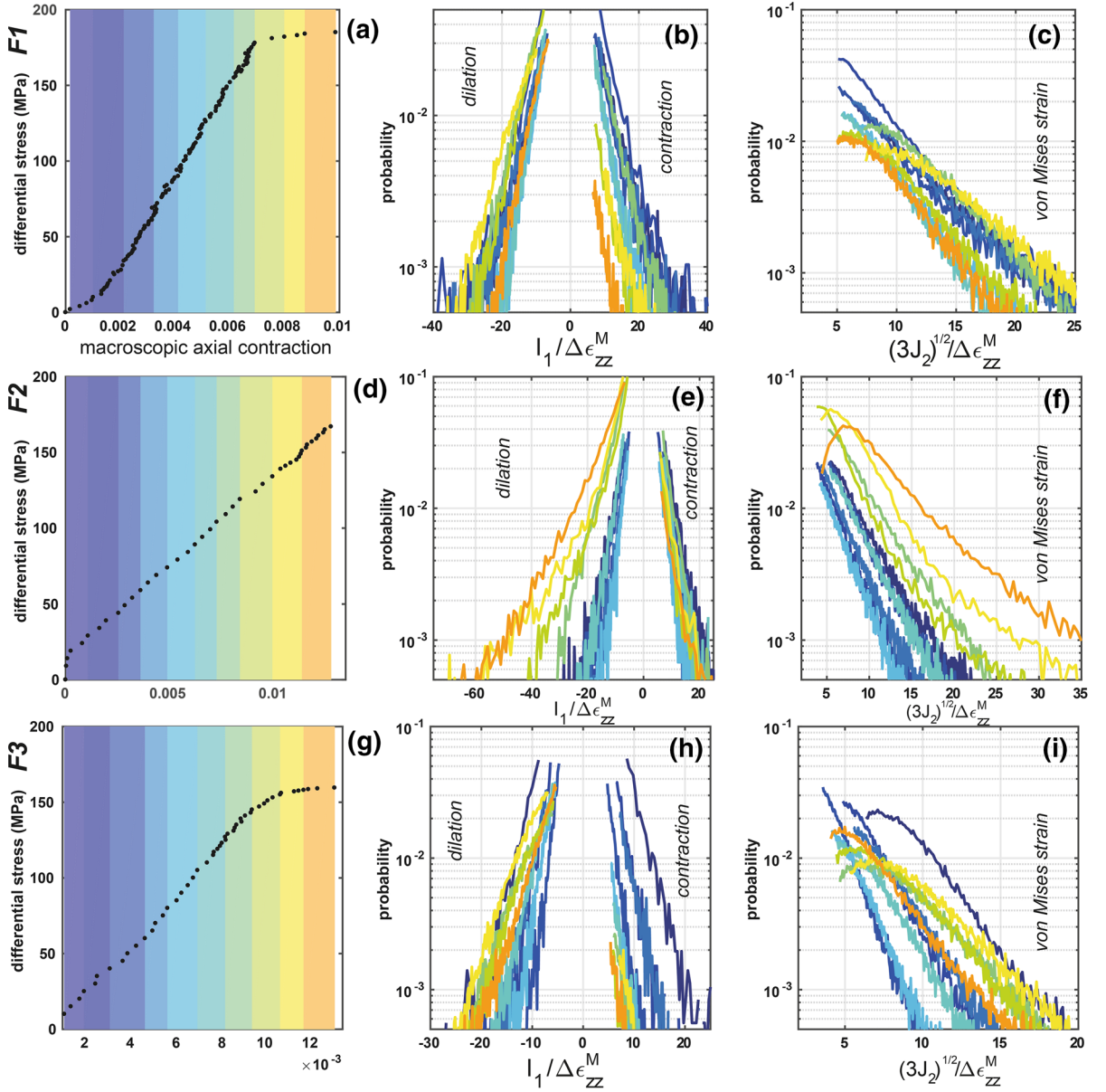
Figure 10
Histograms of incremental normalized strain invariants determined by DVC analysis of pairs of three-dimensional datasets for experiments F1 (**a–c**), F2 (**d–f**), and F3 (**g–i**). **a**, **d**, **g** Differential stress–axial strain curves. The rectangles show the strain intervals between which we performed digital image correlation. **b**, **e**, **h** Histograms of $\frac{I_1(\Delta\varepsilon)}{\Delta\varepsilon_{zz}^{M}}$. **c**, **f**, **i** Histograms of $\frac{(3J_2(\Delta\varepsilon))^{1/2}}{\Delta\varepsilon_{zz}^{M}}$. The color of each histogram corresponds to the strain interval displayed in the first column. The gap in the histogram curves at small magnitudes arises because strain values below the identified threshold (Fig. 3) were removed

invariant of the incremental strain, $I_1(\Delta\varepsilon)$, divided by $\Delta\varepsilon_{zz}^{M}$, and the square root of the von Mises incremental strain, $(3J_2(\Delta\varepsilon))^{1/2}$, divided by $\Delta\varepsilon_{zz}^{M}$ (Fig. 10). Because the incremental normalized strain invariants

$\frac{I_1(\Delta\varepsilon)}{\Delta\varepsilon_{zz}^{M}}$ and $\frac{(3J_2(\Delta\varepsilon))^{1/2}}{\Delta\varepsilon_{zz}^{M}}$ were calculated at many locations (> 50,000 points per tomogram pair), they provided additional information about deformation within the sandstone specimens that global measures such as

porosity, macroscopic axial and radial strains, and the damage index do not capture. In addition, because $\frac{I_1(\Delta\varepsilon)}{\Delta\varepsilon_{zz}^{\mathrm{M}}}$ and $\frac{(3J_2(\Delta\varepsilon))^{1/2}}{\Delta\varepsilon_{zz}^{\mathrm{M}}}$ are measures of incremental strain between two tomogram acquisitions, their mean and median values may not systematically increase as failure is approached.

The evolution of the incremental normalized strain invariants were similar in experiments F2 and F3, but differed from that observed in experiment F1 (Fig. 10). In experiments F2 (Fig. 10b) and F3 (Fig. 10h), the area under the dilatational portion of the $\frac{I_1(\Delta\varepsilon)}{\Delta\varepsilon_{zz}^{\mathrm{M}}}$ histogram increased by more than 200% as the differential stress increased, while the area under the contractional portion did not increase as much. The evolution of $\frac{(3J_2(\Delta\varepsilon))^{1/2}}{\Delta\varepsilon_{zz}^{\mathrm{M}}}$ was similar to that of the contractional part of $\frac{I_1(\Delta\varepsilon)}{\Delta\varepsilon_{zz}^{\mathrm{M}}}$ in these experiments in that, with increasing differential stress, the $\frac{(3J_2(\Delta\varepsilon))^{1/2}}{\Delta\varepsilon_{zz}^{\mathrm{M}}}$ population included a higher proportion of higher-magnitude values, increasing the area under the positive portion of the histogram. In contrast, in experiment F1, the trend of increasing $\frac{I_1(\Delta\varepsilon)}{\Delta\varepsilon_{zz}^{\mathrm{M}}}$ and $\frac{(3J_2(\Delta\varepsilon))^{1/2}}{\Delta\varepsilon_{zz}^{\mathrm{M}}}$ was not as consistent as in the other experiments. In particular, the second to last differential strain increment (yellow in Fig. 10a–c), included more high normalized dilatational strain increments, $\frac{I_1(\Delta\varepsilon)}{\Delta\varepsilon_{zz}^{\mathrm{M}}}$, than the final differential stress increment (orange in Fig. 10a–c), so there was a smaller area under the dilatational portion of the $\frac{I_1(\Delta\varepsilon)}{\Delta\varepsilon_{zz}^{\mathrm{M}}}$ curve. Similarly, the second to last differential strain increment produced a higher area under the $\frac{(3J_2(\Delta\varepsilon))^{1/2}}{\Delta\varepsilon_{zz}^{\mathrm{M}}}$ curve than the final differential strain increment, indicating a higher magnitude of overall shear strain (Fig. 10c). The difference in behavior could be related to the difference of loading path, since the confinement was decreased as failure was approached in experiment F1 but remained constant in experiments F2 and F3 (Fig. 1). To summarize the results of Fig. 10: for samples F1 and F3, most of the strain in the sample was accommodated by local dilation events that we relate to the opening of grain boundaries, whereas for sample F2, the road to failure was due to a combination of dilation and shear as a fault zone developed.

To synthesize these changes in the overall magnitude of each incremental strain field, we summed the dilatational (negative) and contractive (positive) portions of the $\frac{I_1(\Delta\varepsilon)}{\Delta\varepsilon_{zz}^{\mathrm{M}}}$ populations, and the $\frac{(3J_2(\Delta\varepsilon))^{1/2}}{\Delta\varepsilon_{zz}^{\mathrm{M}}}$ populations. These sums document the total normalized strain increments in the sample during loading. We report these sums normalized by the sum calculated for each population in the first differential stress increment (Fig. 11a–c). Figure 11 shows that the relationships between the sums of the incremental contractions, incremental dilations, and von Mises incremental stresses and the macroscopic axial contraction were complex. The trends in experiments F1 and F3 were more similar to each other than they were to experiment F2, as might be expected from the early yielding in experiment F2. In all three experiments, the dilatational $\frac{I_1(\Delta\varepsilon)}{\Delta\varepsilon_{zz}^{\mathrm{M}}}$ sum began to increase when the axial contraction reached about 6×10^{-3}. However, in experiments F1 and F3, the dilatational $\frac{I_1(\Delta\varepsilon)}{\Delta\varepsilon_{zz}^{\mathrm{M}}}$ sum reached a maximum after the yield point had been reached and decreased before failure occurred, whereas in experiment F2, the yield point was reached before the dilatational $\frac{I_1(\Delta\varepsilon)}{\Delta\varepsilon_{zz}^{\mathrm{M}}}$ sum began to increase, and there was no maximum before failure. The sums of $\frac{(3J_2(\Delta\varepsilon))^{1/2}}{\Delta\varepsilon_{zz}^{\mathrm{M}}}$ in experiments F1 and F3 did not change much and stayed around a value of 1. In contrast, in experiment F2, where dilatational and shear strain localized into a core-spanning fracture, the $\frac{(3J_2(\Delta\varepsilon))^{1/2}}{\Delta\varepsilon_{zz}^{\mathrm{M}}}$ sum increased by about a factor of two.

To track the overall strain increments, we extracted the number of local incremental strain values above a threshold (Fig. 11d–f), and then normalized by the sum calculated for each population in the first differential stress increment. The evolution of this quantity is similar to that of the sum of the increments shown in Fig. 11a–c.

The evolution of the spatial distributions of the normalized incremental strain invariants (Fig. 9) illuminates the morphology of the coalescing microfractures that produced the trends observed in the histograms and sums. Consistent with the
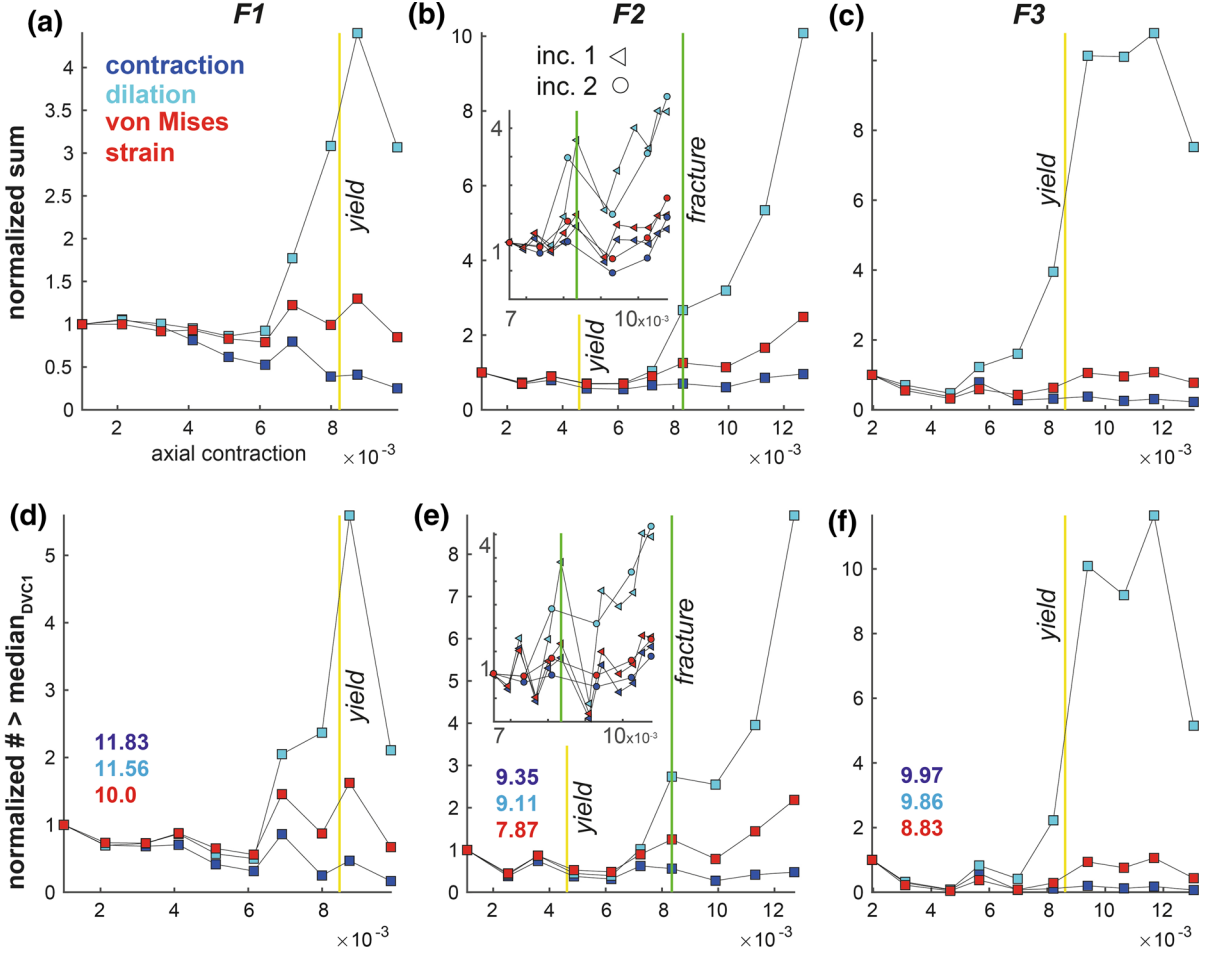
Figure 11

Evolution of sums of incremental strain invariants (**a**–**c**) and number of values above the median identified in the first increment, median$_{\text{DVC1}}$, (**d**–**f**) in experiments F1 (**a**, **d**), F2 (**b**, **e**), and F3 (**c**, **f**). Dark-blue, light-blue, and red squares show values of contractive $\frac{I_1(\Delta\varepsilon)}{\Delta\varepsilon_{zz}^{M}}$, dilatational $\frac{I_1(\Delta\varepsilon)}{\Delta\varepsilon_{zz}^{M}}$, and $\frac{(3J_2(\Delta\varepsilon))^{1/2}}{\Delta\varepsilon_{zz}^{M}}$ (shear strain). Each sum is normalized by the sum calculated in the first increment. Each number of strain values above median$_{\text{DVC1}}$ is normalized by that number in the first increment. Inset of (**b**) shows sums near the yield point of experiment F2 where DVC analyses were performed on 12 pairs of tomograms with successive stress step increase. Yellow lines show the yield point for each experiment. The green line shows the onset of fracture development in sample F2. The value of median$_{\text{DVC1}}$ for each strain invariant population is shown in each of the plots, corresponding to the normalized incremental strain invariant. The dark-blue, light-blue, and red numbers indicate the median values of contraction, dilation, and von Mises incremental strains, respectively

evolution of the contractive vales of $\frac{I_1(\Delta\varepsilon)}{\Delta\varepsilon_{zz}^{M}}$ observed in the histograms and sums, high values of contractive $\frac{I_1(\Delta\varepsilon)}{\Delta\varepsilon_{zz}^{M}}$ did not localize within or around the fracture. This lack of localization of the contractive $\frac{I_1(\Delta\varepsilon)}{\Delta\varepsilon_{zz}^{M}}$ values produced only small changes in the sums and histogram shape, whereas the opening of and slip along fractures produced fracture-localized dilation and shear strain, thus increasing the sums and areas

under the dilatational portion of the $\frac{I_1(\Delta\varepsilon)}{\Delta\varepsilon_{zz}^{M}}$ histogram and the $\frac{(3J_2(\Delta\varepsilon))^{1/2}}{\Delta\varepsilon_{zz}^{M}}$ histogram.

To track the interplay between dilatation, contraction, and shear strain, we show the dilative part of $I_1(\Delta\varepsilon)$, the contractive part of $I_1(\Delta\varepsilon)$, and $(3J_2(\Delta\varepsilon))^{1/2}$, without normalization by $\Delta\varepsilon_{zz}^{M}$, as a function of each value (Fig. 12). The curves outline pairs of strain values with a bivariate kernel density >
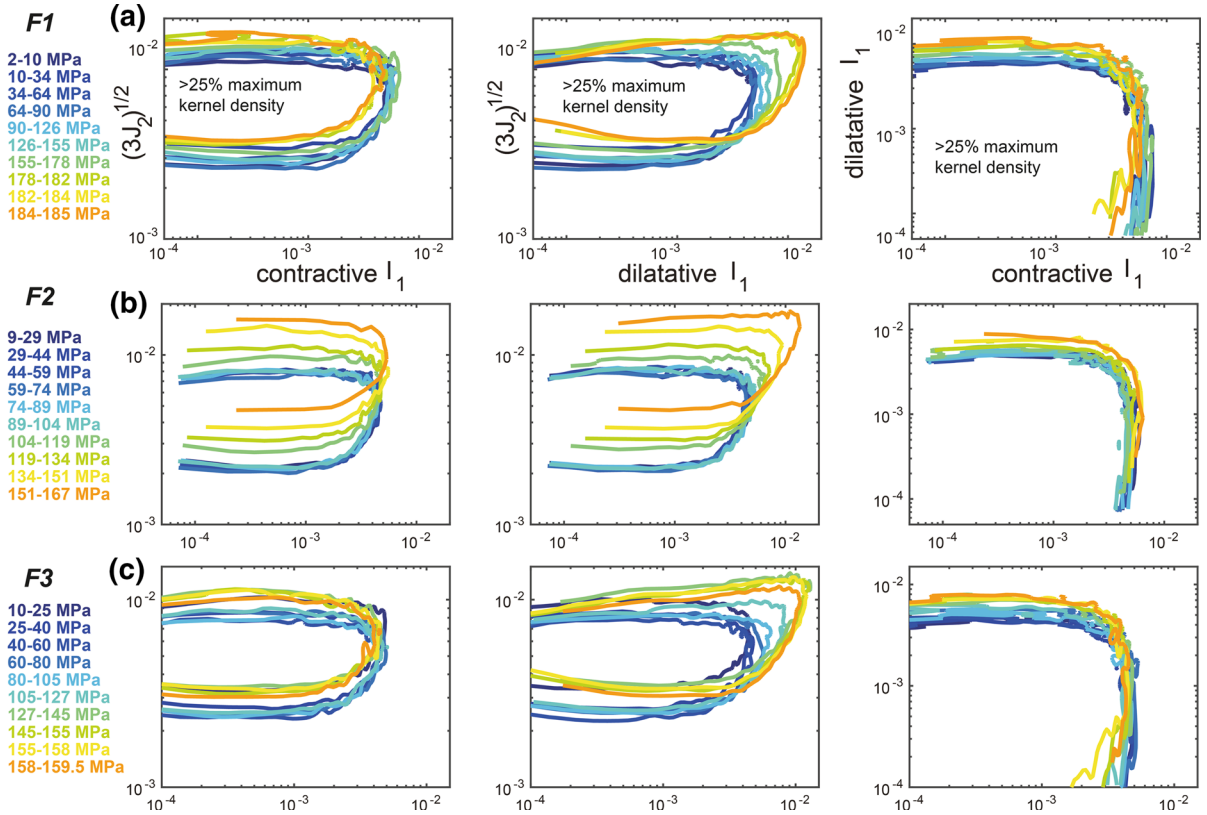
Figure 12
Evolution of deviatoric and normal incremental strain invariants for experiments F1 (**a**), F2 (**b**), and F3 (**c**). For each incremental strain field, we calculated the dilative $\frac{I_1(\Delta\varepsilon)}{\Delta\varepsilon_{zz}^{M}}$, contractive $\frac{I_1(\Delta\varepsilon)}{\Delta\varepsilon_{zz}^{M}}$, and $\frac{(3J_2(\Delta\varepsilon))^{1/2}}{\Delta\varepsilon_{zz}^{M}}$ value at each point. The bivariate kernel density of each pair of strain values was estimated assuming a Gaussian distribution: contractive $\frac{I_1(\Delta\varepsilon)}{\Delta\varepsilon_{zz}^{M}}$ versus $\frac{(3J_2(\Delta\varepsilon))^{1/2}}{\Delta\varepsilon_{zz}^{M}}$ (left), dilative $\frac{I_1(\Delta\varepsilon)}{\Delta\varepsilon_{zz}^{M}}$ versus $\frac{(3J_2(\Delta\varepsilon))^{1/2}}{\Delta\varepsilon_{zz}^{M}}$ (middle), and contractive $\frac{I_1(\Delta\varepsilon)}{\Delta\varepsilon_{zz}^{M}}$ versus dilative $\frac{I_1(\Delta\varepsilon)}{\Delta\varepsilon_{zz}^{M}}$ (right). Lines outline the strain values with a kernel density > 25% of the maximum kernel density

25% of the maximum kernel density. For the three specimens, these data show that: (1) incremental dilation increased much more than incremental compaction as failure was approached, (2) shear strain increased as failure was approached, and (3) the increase in shear strain acted in concert with dilation and was not strongly correlated with contraction (Fig. 12).

5. Discussion

5.1. Micromechanical Models of Brittle Failure

Micromechanical models including the wing-crack model, the pore-emanated crack model, the Hertzian fracture concept, and the pore collapse model have linked grain-scale microscopic processes to macroscopic strain in rocks (see Sect. 2.2). Pore collapse was not observed in the tomograms of these experiments, so the pore collapse model may not adequately describe the failure of these Fontainebleau sandstone specimens. Development of mode I cracks and their dilation preceded the onset of strain localization (samples F1 and F3, Fig. 11a, c) or coincided with this localization (sample F2, Fig. 11b), indicating that relatively high magnitudes of dilation began to localize before high magnitudes of shear strain. We found no evidence for wing crack formation. Wing cracks develop through localized shear displacement that then produces regions of high

tensile stresses, so we would expect to observe localized high shear strain regions before localized dilatational regions in the DVC data, rather than the observed opposite trend. In addition, visual inspection of the tomograms, before and after segmentation, provided no evidence for wing cracks, though it is possible that wing cracks with apertures that were too small to detect were formed.

The pore-emanated crack model, in which cracks open along grain boundaries, could be consistent with the experimental observations of microscale strain due to opening of grain boundaries (Fig. 7e, f). However, the Hertzian fracture concept also matches the experimental observations of the development of transgranular cracks that develop within grains, which the pore-emanated crack model does not predict. The Hertzian fracture concept uses the maximum tangential tensile stress within the contact area between spherical grains to predict grain-scale failure that leads to macroscopic failure (Johnson 1982). Consistent with this concept, we observed that, at small differential stresses, a higher number of intergranular fractures than transgranular fractures developed. Then, as the differential stress increased, and particularly after the yield stress was reached, transgranular fracturing began to dominate deformation until extensive grain comminution occurred (Figs. 4, 5). During early-stage deformation, intergranular fractures may preferentially develop instead of transgranular fractures because the cement that binds sandstone grains may be weaker under tension than the intact grains. Consequently, intergranular fractures may be able to propagate under lower differential stresses than transgranular fractures. In addition, as the differential stress increases, the effect of the difference in strength between the cement and the grains may diminish as preexisting pores close and intergranular contacts are clamped shut under higher normal stresses.

The geometry and volume of the pore network play an important role in controlling the deformation and failure of sandstones because the concentration of tensile stress near pore surfaces initiates the growth of fractures. For a spherical cavity under a compressive uniaxial far-field stress embedded in homogeneous isotropic linear elastic material (e.g., Goodier 1933; Sadowsky and Sternberg 1949; Eshelby 1957; Mura 1982), the stress at the surface of the cavity depends only on the far-field stress and the polar angle, θ, relative to the direction of σ_1. As this angle varies from $\pi/2$ at the equator of the pore to 0 or π at the poles, the resulting compressive stress at the pore surface decreases and becomes tensile near the poles. Because mineral grains and cement are weaker under tensile stress than under compressive stress, fractures are expected to nucleate near the poles of a spherical cavity and propagate preferentially along planes that are oriented subparallel to σ_1. Shear fractures may nucleate at cavity walls at orientations parallel to σ_1, and then propagate at angles that are oblique to σ_1 (Davis et al. 2017). These analytical and modeling approaches have been extended to plastic materials (Monchiet et al. 2008), multiple voids (Tandon and Weng 1986), and polygonal voids. However, exact results cannot usually be obtained, and the effects of the necessary approximations are challenging to assess. Our experiments provide additional insights because these three-dimensional data show that pores have shapes that differ from the spherical geometry often assumed in numerical models (Fig. 7).

Numerical methods such as finite element models (e.g., Eggers et al. 2006; Avazmohammadi and Naghdabadi 2013) and boundary element models (Davis et al. 2017), as well as micromechanical modeling coupled with analogue experiments (Sammis and Ashby 1986), provide additional insights that complement analytical approximations; For example, Nadimi et al. (2015) conducted two-dimensional finite element model simulations of the compression of Fontainebleau sandstone. In these simulations, load-bearing columns developed subparallel to the direction of the compressive stress, consistent with finite element simulations performed by Nadimi et al. (2015), and a model of the failure of brittle porous solids proposed by Sammis and Ashby (1986). In our experimental work, we also observed the formation of subvertical (subaxial) columns separated by subvertical fractures (Figs. 5, 6, 7g–i). However, the columns did not become well developed until vertical strains were substantially larger than those used in the simulations of Nadimi et al. (2015). The geometric difference between the two-dimensional model and the three-dimensional experiment, the strength of the simulated cement bonds, and the nondetection of

fractures with small aperture widths in our X-ray microtomography experiments may have produced this apparent discrepancy between the experiments and the simulations. Features with characteristic scales below the resolution of X-ray microtomography, such as flaws within pore surfaces, mineral grains, and cement, play an important role in the nucleation of microfractures.

5.2. Dilation and Acceleration of Damage When Approaching Failure

In our Fontainebleau sandstone specimens, the total damage, D_ϕ, accelerated toward failure (Fig. 8a) and occurred concomitantly with dilation. In a study of crystalline rock, the damage accelerated as a power law of the normalized stress, $\Delta = \frac{\sigma - \sigma_f}{\sigma_f}$, where σ_f is the differential stress at failure, such that $D_\phi \sim \frac{1}{\beta - 1}[\Delta^{-(\beta - 1)} - 1]$ with an exponent β between 1.4 and 1.8 (Fig. 5 in Renard et al. 2018). In these experiments, the cumulated damage was measured, so that the power-law exponent is $-(\beta - 1)$, where β is the exponent that characterized the power-law divergence of the rate at which the damage increases with increasing differential stress as failure is approached. Based on two-dimensional simulations of uniaxial compression with no confining pressure, Girard et al. (2010) found evidence for power-law divergence of the damage correlation length with decreasing Δ as Δ approached failure, thus suggesting that failure is a critical phenomenon. This model of brittle failure indicates that elastic interactions between developing fractures over long-range, system-size, distances can explain the power-law divergence of incremental damage as Δ decreases toward failure in low-porosity crystalline rock (Girard et al. 2010). A power-law acceleration of acoustic emission prior to failure was also observed in the deformation of heterogeneous materials (Vasseur et al. 2015).

In contrast, in our experiments on Fontainebleau sandstone, the acceleration of damage occurred at a slower than power-law rate (Fig. 8b). This slower acceleration of damage may occur in more porous rocks compared with crystalline rocks because, when the propagating tip or edge of a microfracture reaches a pore, the local stress concentrations at the fracture tip or edge diminish. This may prevent further propagation of the fracture until the local stress field increases. Although the rate of damage accumulation differed in our recent monzonite experiments (Renard et al. 2018) and these sandstone experiments, in all five experiments (three sandstone and two monzonite experiments) we observed an acceleration of damage as failure was approached. This acceleration of damage was a precursor to shear failure in our experiments, as rock damage models (Lyakhovsky et al. 1997; Dahmen et al. 2009; Girard et al. 2010) and acoustic emission experiments on sandstones (Cox and Meredith 1993; Wu et al. 2000; Schubnel et al. 2007; Fortin et al. 2009; Nasseri et al. 2014; Ghaffari et al. 2014; Goodfellow et al. 2015) indicate. Our analysis reveals that this damage increase is slower than the power-law divergence predicted by some damage models (Fig. 8). Furthermore, this analysis is the first to separate this damage increase into new microfracture development and pore dilation (Fig. 6a). Segmentation of X-ray tomograms enabled this distinction because it captures aseismic and seismic strain, whereas acoustic emissions record only seismic strain.

Proposed micromechanical models of failure of porous sedimentary rock depend on the processes that produce opening-mode failure and dilation at the grain scale. In particular, the global evolution of D_ϕ likely differs between porous and crystalline rocks because of the pervasive pore network in more porous rocks. Macroscopic dilation has been observed during the deformation of low-porosity crystalline rocks (e.g., Brace 1978) and porous sedimentary rocks (e.g., Baud et al. 2000). However, the degree of dilation in porous sedimentary rocks differs from that in crystalline rocks because, in porous rocks, microfractures may nucleate at grain boundaries, break them, and cause pore collapse (e.g. Handin et al. 1963; Wong et al. 1997). In our Fontainebleau sandstone experiments, the majority of cracks nucleated at grain contacts and opened along grain boundaries (Fig. 7), similar to the findings of some other studies on sandstones (Menéndez et al. 1996; Wu et al. 2000). Some cracks also propagated through grains, as observed in other studies (Handin et al. 1963; Zhang et al. 1990; Wu et al. 2000; El Bied et al. 2002). The tomograms do not

reveal clear compaction or pore collapse at the grain scale prior to failure. Although there was a global axial shortening of the sample, the overall porosity increased from the onset of yield to failure. The low initial porosity of this rock (5–7%) may have inhibited pore collapse because the potential maximum tensile stress that may develop at pore surfaces decreases with decreasing pore volume (e.g., Wong and Baud 2012).

5.3. Implications of DVC Strain Analysis

Videos S3–S5 show that some high values of strain were detected by DVC analysis inside the sample from the beginning of loading. This could be related to the presence of weak zones inside the samples that deformed even under low differential stress. Such behavior has also been observed when acoustic emissions were used to monitor deformation in porous sandstones (e.g., Fortin et al. 2009).

The more diffuse distribution of the high incremental strains in experiments F1 and F3 (Fig. 9a, c, Videos S3 and S5) compared with experiment F2 (Fig. 9b, Video S4) suggests why the sums of the incremental von Mises strains did not change as significantly in experiments F1 and F3 compared with experiment F2 (Fig. 11). A core-spanning fracture did not develop prior to macroscopic failure in these experiments as it did in experiment F2. Instead, preceding macroscopic failure, the high values of the incremental strain remained relatively diffuse, although there was some localization of the high strain values into tighter clusters (Fig. 9a) and narrower bands (Fig. 9c) preceding macroscopic failure. Consequently, much of the high incremental strain population remained outside of these strain localization zones preceding macroscopic failure. However, propagation, opening, and sliding along faults produced the final stage of macroscopic failure in all three experiments. This suite of observations is similar to what was observed in experiments that monitored acoustic emissions (e.g. Wu et al. 2000; Fortin et al. 2009) and in which a surge of acoustic emissions occurred from the yield point to failure in sandstones during brittle deformation. The DVC analyses of experiments F1 and F3 show that strain events occurred homogeneously in the volume

(Videos S3 and S5), similar to the cataclastic compaction of a porous sandstone (top panel of Fig. 5 in Fortin et al. 2009) and was attributed to the opening of microfractures along grain boundaries (Menéndez et al. 1996). The DVC analysis of experiment F2, in which a fault developed, is also similar to observations of shear localization in a porous sandstone (middle panel of Fig. 5 in Fortin et al. 2009; Wu et al. 2000). In contrast to the experiments of Fortin et al. (2009), we did not observe pore collapse in the tomography data and our DVC results do not show significant volumetric compaction, likely due to the low porosity of the Fontainebleau sandstone that we investigated.

The evolving distribution of the higher incremental strain magnitudes revealed by the DVC analyses of experiment F2 indicates that both dilation and shear strain localized along the core-spanning fracture (Fig. 9b). The incremental strain fields suggest that, for differential stresses of 104 MPa to 151 MPa, incremental dilatational strains dominated the strain field surrounding and within the developing shear fault zone, and above 151 MPa, incremental shear strain became more localized than dilatational strains around the developing fault zone (Figs. 9b, S3). These observations are consistent with post mortem scanning electron microscopy images of deformed sandstones that showed shear cracks dominating within the fault zone (e.g., Wu et al. 2000). Initially, dilation, and perhaps tensile failure, localized along the incipient fault zone, and then localized shear strain occurred within the developing fault only after some dilation occurred.

To investigate in more detail the dominant failure modes that facilitated the initiation of the fracture observed in F2, we calculated the incremental strain fields following the yield point with the highest possible temporal (differential stress) resolution. Comparing the distribution of the high differential strain magnitudes above the 95th percentile, or the top 5% of values, indicated that the high magnitudes of dilatational $\frac{I_1(\Delta\varepsilon)}{\Delta\varepsilon_{zz}^M}$ began to concentrate around the protofracture before the high magnitudes of $\frac{(3J_2(\Delta\varepsilon))^{1/2}}{\Delta\varepsilon_{zz}^M}$ (Fig. S3). This observation is consistent with the more localized distribution of dilatational $\frac{I_1(\Delta\varepsilon)}{\Delta\varepsilon_{zz}^M}$

relative to the spatial distribution of $\frac{(3J_2(\Delta\varepsilon))^{1/2}}{\Delta\varepsilon_{zz}^M}$ from 104–151 MPa, and the more localized distribution of $\frac{(3J_2(\Delta\varepsilon))^{1/2}}{\Delta\varepsilon_{zz}^M}$ relative to dilatational $\frac{I_1(\Delta\varepsilon)}{\Delta\varepsilon_{zz}^M}$ from 151–167 MPa observed in the lower temporal resolution analysis (Fig. 9). The evolution of the sums above the yield point (insets in Fig. 11b, e) indicate that the normalized sum of $\frac{(3J_2(\Delta\varepsilon))^{1/2}}{\Delta\varepsilon_{zz}^M}$ is generally slightly higher than the normalized sum of the dilatational part of the $\frac{I_1(\Delta\varepsilon)}{\Delta\varepsilon_{zz}^M}$ field in the differential stress increments immediately preceding the yield point. These properties of the dilatational $\frac{I_1(\Delta\varepsilon)}{\Delta\varepsilon_{zz}^M}$ began to exceed those of the $\frac{(3J_2(\Delta\varepsilon))^{1/2}}{\Delta\varepsilon_{zz}^M}$ when dilatational strains began to localize along the core-spanning fracture (109–114 MPa differential stress in Fig. 9; green lines in Fig. 11).

In the two experiments (F2 and F3) in which the incremental strain invariant sums generally increase (Fig. 11), and the areas under the histograms generally increase (Fig. 10), the cumulative strain magnitude distributions generally progressed toward higher strain magnitudes with increasing differential stress (Fig. S4). In experiment F1, this trend was less consistent than in the other experiments. In particular, the magnitude–frequency distributions shifted toward lower magnitudes of strain from the second to last differential stress increment to the final differential stress increment, consistent with the observed decrease in the sums (Fig. 11).

To characterize the distribution of strain magnitudes close to the macroscopic shear failure, we searched for scaling relationships within the populations of normalized incremental dilatational $\frac{I_1(\Delta\varepsilon)}{\Delta\varepsilon_{zz}^M}$, contractional $\frac{I_1(\Delta\varepsilon)}{\Delta\varepsilon_{zz}^M}$, and $\frac{(3J_2(\Delta\varepsilon))^{1/2}}{\Delta\varepsilon_{zz}^M}$ strain increments shown in Fig. 10. Such scaling relationships may reflect the long-range elastic interactions of the stress field produced by individual local microfractures and the presence of initial mechanical heterogeneities (e.g., Renard et al. 2018). The cumulative frequency distributions of the incremental strain invariants show a linear trend on a log–log scale covering 1–2 orders of magnitude (Fig. S4). The incremental strain invariant curves flatten toward lower magnitudes

near the resolution limit of the incremental strain measurements, below which the values were removed (Fig. S4). The linear trend is indicative of a power-law scaling behavior with numerous small incremental strain values, and fewer large incremental strain values. In log–log space, the slope $(\beta + 1)$ of the cumulative histogram gives the exponent of the power-law scaling relationship, β, of the strain increments (Fig. S5). We calculated the power-law exponents using the maximum-likelihood approach of Clauset et al. (2009). These exponents varied during the loading in the three experiments (Fig. S5). However, we observed no significant trend in the exponent value throughout deformation. This relative stability of the exponents could be due to the small range of spatial scales over which effective power-law behavior was observed (Fig. S4).

5.4. Transition from Microfracture Coalescence to Localized Shear Failure

The SEM images revealed that, after a distinct shear band formed in experiment F2, extensive grain comminution produced a layer of gouge within the shear zone (Fig. 7). The time resolution of the experiments (~ 1.5 min between scans) prevented determination of whether the core-spanning fracture in experiment F2 developed through (1) a localized nucleation and propagation mechanism or (2) the formation of a dense array of microfractures that coalesced and ultimately formed a volume of unconsolidated, comminuted granular material. Tomograms acquired beyond the yield point of experiment F2 showed progressive nucleation, growth, and coalescence of an array of opening cracks oriented subparallel to σ_1 (Figs. 5, 7g–i).

Mechanical breakdown within rupture zones may initially produce a sand-like granular material at these confining stresses. As comminution broadens the grain size distribution within a shear zone, the local shear zone porosity may decrease as small grains fill spaces between larger grains. The rounding and reorientation of large survivor grains (Cladouhos 1999) may also contribute to porosity reduction in shear zones following larger shear displacements. Such shear zone gouges may also enable local dilation. However, the development of

unconsolidated sand grains in the shear zone alone cannot produce the observed macroscopic dilation (negative macroscopic volumetric strain) of about − 0.15 following failure. This macroscopic dilation of the specimen suggests that microfractures in the material surrounding the shear zone contributed to the postfailure porosity, in addition to dilation within the shear zone.

In experiments in which unconsolidated granular material was subjected to shear deformation with confining stress perpendicular to the shear plane, shear bands developed with enhanced comminution (e.g., Marone and Scholz 1989). When a broad grain size distribution developed within the fault gouge, the local porosity within the gouge decreased (Marone and Scholz 1989). In the case of the low-porosity Fontainebleau sandstone used in the experiments reported here, dilation occurred within the incipient shear rupture zone because of the formation of a dense array of subvertical microfractures (Fig. 6). The opening of these microfractures may lead initially to the formation of a high-porosity band of unconsolidated quartz particles that evolves into a low-porosity zone of highly comminuted quartz particles with a broad size distribution. However, we did not observe a low-porosity zone in these experiments, perhaps because the shear strain within the rupture zone and/or the confining stress perpendicular to the shear plane were too small to reorient, round, or crush the grains within the incipient fault gouge, and thereby decrease porosity within the zone. Perhaps if we had continued the experiment beyond macroscopic failure and allowed more evolution of the fault gouge within the shear zone, the local porosity within the gouge would have decreased. In additional, the short (multiple hour) time span and dry conditions in our experiments prevented chemical processes that would further reduce fault zone porosity in the crust.

Differences in the rate of fracture coalescence and fault propagation may have caused a core-spanning fracture to localize earlier in experiment F2 (closer to the yield point) than experiments F1 and F3 (immediately before macroscopic failure). For the same rate of deformation, fault propagation tends to progress at a slower rate in more macroscopically brittle rocks than in less brittle rocks that have a higher component of ductile deformation (Ougier-Simonin and Zhu 2013, 2015). The imposed confining stress of experiment F1 (20 MPa) was larger than that of experiment F2 (10 MPa), and the nominal strain rate of experiment F1 (184 scans, each of 1.5 min duration) was lower than that of experiment F2 (49 scans, each of 1.5 min duration). Higher confining stresses and lower strain rates tend to allow more ductile deformation to accommodate the applied strain, and rocks behave in a less brittle manner with lower fault propagation rates. Consequently, the experimental conditions produced more brittle behavior in experiment F2 than in experiment F1, which promoted slower fault propagation in experiment F2 compared with experiment F1. Similarly, fault propagation may have occurred at slower rates in experiment F2 than experiment F3 because the Young's modulus and failure stress of experiment F3 were lower than those of experiment F2, signaling more brittle behavior during experiment F2 than F3.

In each of our experiments, the angle of inclination, θ, between the maximum compression direction and the core-spanning fracture was smaller than that predicted by the Mohr–Coulomb failure criterion. We cannot rule out the possibility that this was caused by the absence of lubrication of the piston–sandstone interface. However, this observation was also reported in previous experiments on Vosges sandstone (22% porosity) in which failure occurred via propagation of subaxial fractures (e.g., Bésuelle et al. 2000). In these experiments, increasing confining stress increased the orientation of the through-going fractures with respect to σ_1. At the highest confining pressures, compaction bands developed subperpendicular to σ_1, thereby following the observed trend. The subaxial microfractures appeared to control how strain localized into core-spanning fractures. As the density of subvertical microfractures increased, the mechanical properties of the rock became increasingly anisotropic, which may have modified the orientation of new fractures and how fractures coalesced. These fractures had orientations between mode I subaxial fractures when $P_c \ll \sigma^f$, and shear failure consistent with the orientation predicted by the Mohr–Coulomb failure criterion when $P_c < \sigma^f$ (i.e., when P_c is a few tens of MPa), where σ^f is the differential stress at failure. As the differential stress

increased and the subaxial fractures increased in size, the unfractured columns between them became more unstable (e.g., Fig. 41 in Peng and Johnson 1972). If one column collapses, the forces acting on it will be transferred to other columns, and a cascade of column collapses may be responsible for strain localization that forms fractures at higher angles than those predicted by the Mohr–Coulomb criterion. Such conceptual description of the failure process is quantified in statistical physics models. As failure is approached, the sizes of the cascades (or avalanches) will increase in size as observed in numerical simulations (e.g., Dahmen et al. 2009; Girard et al. 2010). The preferential orientation of subaxial microfractures suggests that the long-range function that describes how the rate of damage evolution at one point influences the damage evolution at other points should depend on both the direction and length of the vector between the two points because damage develops preferentially in certain directions, and is thus anisotropic, as proposed for crystalline rocks in the model of Lockner and Madden (1991).

The final core-spanning fault in our experiments was not planar, but curved (Figs. 5d, 6d). Such curved fault surfaces have also been observed in crystalline rocks (Peng and Johnson 1972). Curved strain concentration zones are not uncommon; For example, Sulem and Ouffroukh (2006) mentioned measuring the orientation of the shear band on the central part of the specimen because the shear band often warps close to the extremities.

The development of a new micromechanical model for sandstone is out of the scope of the present study. A sound understanding of the micromechanics of complex materials should help justify the forms of macroscopic constitutive equations that predict the mechanical and rheological behaviors of rocks. Such macroscopic laws are useful because of their small number of parameters (e.g., Rudnicki and Rice 1975; see also the discussion in Dresen and Guéguen 2004) and provide a complementary approach to microme-chanical modeling. A micromechanical constitutive model should incorporate processes that cause the local increase of damage (e.g., opening of grain boundaries and formation of transgranular microfrac-tures) and the effect of damage on the local stress distribution (Cox and Meredith 1993). It should

predict macroscopic properties such as strength, amount of dilation, and evolution of elastic param-eters and also whether a fault will develop early, near the yield point (like the core-spanning fracture in experiment F2) or later, near failure (experiments F1 and F3). However, the materials and experimental conditions were essentially the same in experiments F2 and F3, and this suggests that experiments F2 and F3 were conducted very near the boundary between two quite different deformation and failure regimes or that prediction of deformation and failure will be very challenging if not impossible for rocks like low-porosity Fontainebleau sandstone.

5.5. *Limitations of Digital Volume Correlation Analysis Near Failure*

Our DVC analyses quantified local strain compo-nents (dilation, compaction, shear strain) that may be compared with the evolving pore and fracture network revealed through segmentation of the tomo-grams, and the macroscopic strain. Histograms of incremental strain components (Fig. 10) and the sum of the increments of each strain component (Fig. 11) at increasing differential stress steps showed that components of local strain concentrations can be up to one order of magnitude larger than the macro-scopic axial strain. The power-law scaling analysis of the cumulated distribution of the incremental strain components showed that the exponent did not vary significantly as failure is approached (Fig. S5), whereas the total damage increased (Fig. 8).

During macroscopic failure and the postfailure phase when comminution occurred, the structure of the incipient fault zone changed rapidly. Conse-quently, DVC analysis of the evolution of the incipient fault zone may not produce meaningful results because changes in the sizes, shapes, and orientations of quartz grains, and grain fragmentation, during the acquisition time may blur the tomograms. In addition, large differences in microstructures between tomograms may inhibit adequate correlation of subvolumes across sequential tomograms. Time-lapse X-ray microtomography of deformation with small increments of shear strain could reveal the comminution process within the incipient fault zone in more detail than these experiments. However,

strain fields obtained from DVC analysis of tomograms separated by these small strain increments will have lower signal-to-noise ratios than the strain fields presented in this study because the signal (incremental strain) decreases when the the macroscopic strain between scans decreases (e.g., McBeck et al. 2018).

5.6. Neutron Tomography

Neutron tomography has been used with DVC analysis to investigate strain localization and compressive failure of Bentheim sandstone (Tudisco et al. 2015). However, the technology of neutron tomography is not as far advanced as the technology of X-ray tomography. Neutron microtomography requires several hours for three-dimensional acquisitions at 30 μm spatial resolution, whereas the HADES deformation apparatus installed at beamline ID19 at ESRF enables 1.5 min acquisition times at 6.5 μm spatial resolution for cores 1 cm tall and 0.5 cm wide. Consequently, time-lapse neutron tomography has been only rarely used to investigate the micromechanics of rocks (e.g., Stavropoulou et al. 2018). The attenuation coefficients of neutrons are not as high as those of X-rays, which is an advantage for triaxial rigs with thick walls that are required for applying higher stresses than the 200 MPa differential stress limit of the HADES rig. In addition, neutron and X-ray contrasts are quite different, and in particular, the high neutron cross section of hydrogen would be advantageous when studying fluids such as water and hydrocarbons within rocks.

5.7. Temperatures and Stress Limits

The HADES rig was fabricated from titanium, and experiments can be conducted in the rig at stresses up to 200 MPa and temperatures up to 250 °C. This enables processes that occur at depths up to about 7 km to be investigated. While a very broad range of geological processes and most geotechnical applications occur under these conditions, there is a clear need to extend the range of temperatures and stresses. It should be possible to achieve this by using advanced materials that are strong at high temperatures and have low X-ray

attenuation coefficients. Candidate materials include alloys composed primarily of lithium, beryllium, magnesium, and aluminum, metal-matrix composites formed from these light alloys and carbon or ceramic fibers, and carbon-fiber-reinforced carbon. However, most, if not all, of these and similar materials are difficult and expensive to fabricate, and few companies have experience with the design and manufacture of apparatus constructed from these materials.

6. Conclusions

Segmentation and digital volume correlation analysis of micrometer-resolution tomograms acquired through in situ dynamic synchrotron X-ray microtomography during triaxial compression loading revealed the damage and strain preceding brittle macroscopic failure in three experiments on Fontainebleau sandstone. In one experiment, a system-size fracture nucleated at 78% of the differential stress at failure and accommodated an increasing proportion of incremental shear strain relative to incremental dilatational strain. In the other two experiments, opening of grain boundaries was the dominant dilation mechanism and localization occurred later, at 95% of the differential stress at failure. Increases in dilatancy and shear strain at the micro- and macroscales were observed during the loading stage preceding failure for all three experiments.

Our experiments are consistent with experiments performed on Fontainebleau sandstone (El Bied et al. 2002; Schubnel et al. 2007; Nasseri et al. 2014; Goodfellow et al. 2015) and on other sandstones (Handin et al. 1963; Menéndez et al. 1996; Wu et al. 2000; Fortin et al. 2009). Failure of Fontainebleau sandstone did not produce discontinuous shear displacement along an idealized plane separated by two essentially undamaged sandstone bodies. Instead, progressive damage accumulated with increasing differential stress as microfractures propagated along grain boundaries as well as through grains (Videos S1 and S2). After the yield stress was reached, damage accumulated at increasing rates until macroscopic shear failure occurred. The microscopic damage

developed as subaxial fractures that propagated, coalesced, and became increasingly concentrated into a high-aspect-ratio system-spanning volume.

Our experimental approach provided new information on the nucleation of failure and on the transitions between microfracture nucleation, microfracture coalescence, and macroscopic failure. Incremental strain components revealed by DVC analysis indicated that the high-density subaxial fracture zone did not form a plane but a curved surface. This progressive damage enhanced heterogeneity in the stress and strain fields, as well as the local distribution of mechanical properties. Time-lapse X-ray microtomography and DVC analysis provided detailed information about the evolving microstructure of the Fontainebleau sandstone cylinders as they deformed and approached macroscopic failure. The dilation of the samples during loading was due to both crack opening and pore opening, with an almost equal volumetric contribution of these two processes to the increase of void volume (Fig. 6a). The difference in micromechanical behavior between experiments F1 and F3 on the one hand, and F2 on the other hand did not appear clearly in the stress–strain curves (Fig. 1), which showed that the ability to "look inside" rock specimens provided by X-ray tomography is critical to identify the route to failure. Another important result was obtained by segmenting the voids during loading. We observed a slowdown of the rate at which damage, characterized by the void volume fraction based damage index, D_ϕ, increased with increasing differential stress as failure was approached (Fig. 8), which is not observed in crystalline rocks (Renard et al. 2018). We attribute this to the pinning of microfractures by pores that may reduce the stress concentration at crack tips. These new results demonstrate that very few, if any, other experimental methods enable such precise correlations between the macroscopic mechanical behavior of rock specimens and the micromechanical processes that occur within them.

Acknowledgements

REFERENCES

Andrä, H., Combaret, N., Dvorkin, J., Glatt, E., Han, J., Kabel, M., et al. (2013). Digital rock physics benchmarks—Part I: Imaging and segmentation. *Computers and Geosciences, 50,* 25–32.

Ashby, M. F., & Sammis, C. G. (1990). The damage mechanics of brittle solids in compression. *Pure and Applied Geophysics, 133*(3), 489–521.

Auzerais, F. M., Dunsmuir, J., Ferreol, B. B., Martys, N., Olson, J., Ramakrishnan, T. S., et al. (1996). Transport in sandstone: A study based on three dimensional microtomography. *Geophysical Research Letters, 23*(7), 705–708.

Avazmohammadi, R., & Naghdabadi, R. (2013). Effective behavior of porous elastomers containing aligned spheroidal voids. *Acta Metallurgica, 224,* 1901–1915.

Baud, P., Reuschlé, T., Ji, Y., Cheung, C. S., & Wong, T. F. (2015). Mechanical compaction and strain localization in Bleurswiller sandstone. *Journal of Geophysical Research: Solid Earth, 120,* 6501–6522.

Baud, P., Zhu, W., & Wong, T. F. (2000). Failure mode and weakening effect of water on sandstone. *Journal of Geophysical Research: Solid Earth, 105,* 16371–16389.

Bay, B. K., Smith, T. S., Fyhrie, D. P., & Saad, M. (1999). Digital volume correlation: Three-dimensional strain mapping using X-ray tomography. *Experimental Mechanics, 39*(3), 217–226.

Bésuelle, P., Desrues, J., & Raynaud, S. (2000). Experimental characterisation of the localisation phenomenon inside a Vosges sandstone in a triaxial cell. *International Journal of Rock Mechanics and Mining Science, 37,* 1223–1237.

Bourbie, T., & Zinszner, B. (1985). Hydraulic and acoustic properties as a function of porosity in Fontainebleau sandstone. *Journal of Geophysical Research: Solid Earth, 90*(B13), 11524–11532.

Brace, W. F. (1978). Volume changes during fracture and frictional sliding: A review. *Pure and Applied Geophysics, 116,* 603–614.

Brace, W. F., Paulding, B. W., & Scholz, C. H. (1966). Dilatancy in the fracture of crystalline rocks. *Journal of Geophysical Research, 71*(16), 3939–3953.

Buades, A., Coll, B., & Morel, J. M. (2005). A non-local algorithm for image denoising, in computer vision and pattern recognition. *IEEE Computer Society Conference, 2,* 60–65.

Cladouhos, T. T. (1999). Shape preferred orientations of survivor grains in fault gouge. *Journal of Structural Geology, 21*(4), 419–436.

Clauset, A., Shalizi, C. R., & Newman, M. (2009). Power-law distributions in empirical data. *Society for Industrial and Applied Mathematics Review, 51*(4), 661–703.

Coker, D. A., Torquato, S., & Dunsmuir, J. H. (1996). Morphology and physical properties of Fontainebleau sandstone via a tomographic analysis. *Journal of Geophysical Research: Solid Earth, 101*(B8), 17497–17506.

Cox, S. J. D., & Meredith, P. G. (1993). Microcrack formation and material softening in rock measured by monitoring acoustic emissions. *International Journal of Rock Mechanics and Mining Sciences and Geomechanics Abstracts, 30*(1), 11–24.

Dahmen, K. A., Ben-Zion, Y., & Uhl, J. T. (2009). A micromechanical model for deformation in disordered solids with universal predictions for stress-strain curves and related avalanches. *Physical Review Letters, 102,* 175501.

Davis, T., Healy, D., & Bubeck, A. (2017). Stress concentrations around voids in three dimensions: The roots of failure. *Journal of Structural Geology, 102,* 193–207.

Dresen, G., & Guéguen, Y. (2004). Damage and rock physical properties. In Y. Guéguen & M. Bouteca (Eds.), *Mechanics of fluid-saturated rocks* (pp. 169–217). Amsterdam: Elsevier Academic.

Eggers, C. G., Berli, M., Accorsi, M. L., & Or, D. (2006). Deformation and permeability of aggregated soft earth materials. *Journal of Geophysical Research, 111,* B10204. https://doi.org/10.1029/2005JB004123.

El Bied, A., Sulem, J., & Martineau, F. (2002). Microstructure of shear zones in Fontainebleau sandstone. *International Journal of Rock Mechanics and Mining Sciences, 39,* 917–932.

Eshelby, J. D. (1957). The determination of the elastic field of an ellipsoidal inclusion and related problems. *Proceedings of the Royal Society of London Series A—Mathematical and Physical Sciences, 241,* 376–396.

Faulkner, D. R., Mitchell, T. M., Healy, D., & Heap, M. J. (2006). Slip on 'weak' faults by the rotation of regional stress in the fracture damage zone. *Nature, 444*(7121), 922.

Fortin, J., Stanchits, S., Dresen, G., & Guéguen, Y. (2009). Acoustic emissions monitoring during inelastic deformation of porous sandstone: Comparison of three modes of deformation. *Pure and Applied Geophysics.* https://doi.org/10.1007/s00024-009-0479-0.

Fredrich, J. T., Greaves, K. H., & Martin, J. W. (1993). Pore geometry and transport properties of Fontainebleau sandstone. *International journal of rock mechanics and mining sciences, 30*(7):691–697.

Ghaffari, H. O., Nasseri, M. H. B., & Young, R. P. (2014). Faulting of rocks in a three-dimensional stress field by micro-anticracks. *Scientific Report, 4,* 5011.

Girard, L., Amitrano, D., & Weiss, J. (2010). Failure as a critical phenomenon in a progressive damage model. *Journal of Statistical Mechanics: Theory and Experiment.* https://doi.org/10.1088/1742-5468/2010/01/P01013.

Goodfellow, S. D., Tisato, N., Ghofranitabari, M., Nasseri, M. H. B., Maxwell, S. C., & Young, R. P. (2015). Attenuation properties of Fontainebleau sandstone during true triaxial deformation using active and passive ultrasonics. *Rock Mechanics and Rock Engineering, 48,* 2551–2566.

Goodier, J. N. (1933). Concentration of stress around spherical and cylindrical inclusions and pores. *Journal of Applied Mechanics, 55,* 39–44.

Hall, S. A., Bornert, M., Desrues, J., Pannier, Y., Lenoir, N., Viggiani, G., et al. (2010). Discrete and continuum analysis of localised deformation in sand using X-ray µCT and volumetric digital image correlation. *Géotechnique, 60*(5), 315–322.

Handin, J., Hager, R. V., Friedman, M., & Feather, J. N. (1963). Experimental deformation of sedimentary rocks under confining pressure: Pore pressure tests. *AAPG Bulletin, 47,* 717–755.

Hazzard, J. F., Young, R. P., & Maxwell, S. C. (2000). Micromechanical modeling of cracking and failure in brittle rocks. *Journal of Geophysical Research: Solid Earth, 105,* 16683–16697.

Heap, M. J., & Faulkner, D. R. (2008). Quantifying the evolution of static elastic properties as crystalline rock approaches failure. *International Journal of Rock Mechanics and Mining Sciences, 45*(4), 564–573.

Horii, H., & Nemat-Nasser, S. (1986). Brittle failure in compression: splitting faulting and brittle-ductile transition. *Philosophical Transactions of the Royal Society of London A, 319*(1549), 337–374.

Johnson, K. L. (1982). One hundred years of Hertz contact. *Proceedings of the Institution of Mechanical Engineers, 196*(1), 363–378.

Kanaya, T., & Hirth, G. (2018). Brittle to semibrittle transition in quartz sandstone: Energetics. *Journal of Geophysical Research: Solid Earth, 123,* 84–106.

Katz, O., & Reches, Z. (2004). Microfracturing, damage, and failure of brittle granites. *Journal of Geophysical Research: Solid Earth, 109,* B01206.

Kemeny, J. M., & Cook, N. G. (1991). Micromechanics of deformation in rocks. In *Toughening mechanisms in quasi-brittle materials* (pp. 155–188). Dordrecht: Springer.

Kwiatek, G., Charalampidou, E. M., Dresen, G., & Stanchits, S. (2014). An improved method for seismic moment tensor inversion of acoustic emissions through assessment of sensor coupling and sensitivity to incidence angle. *International Journal of Rock Mechanics and Mining Sciences, 65,* 153–161.

Lindquist, W. B., Venkatarangan, A., Dunsmuir, J., & Wong, T. F. (2000). Pore and throat size distributions measured from synchrotron X-ray tomographic images of Fontainebleau sandstones. *Journal of Geophysical Research: Solid Earth, 105*(B9), 21509–21527.

Lockner, D., Byerlee, J. D., Kuksenko, V., Ponomarev, A., & Sidorin, A. (1991). Quasi-static fault growth and shear fracture energy in granite. *Nature, 350,* 39–42.

Lockner, D. A., Byerlee, J. D., Kuksenko, V., Ponomarev, A., & Sidorin, A. (1992). Observations of quasistatic fault growth from acoustic emissions. In B. Evans & W. F. Brace (Eds.), *Fault mechanics and transport properties of rocks* (Vol. 1, pp. 3–31). Cambridge: Academic Press.

Lockner, D., & Madden, T. (1991). A multiple-crack model of brittle fracture. 1. Non-time-dependent simulations. *Journal of Geophysical Research, 96,* 19623–19642.

Louis, L., Wong, T. F., & Baud, P. (2007). Imaging strain localization by X-ray radiography and digital image correlation: Deformation bands in Rothbach sandstone. *Journal of Structural Geology, 29*(1), 129–140.

Lyakhovsky, V., Ben-Zion, Y., & Agnon, A. (1997). Distributed damage, faulting, and friction. *Journal of Geophysical Research: Solid Earth, 102,* 27635–27649.

Marone, C., & Scholz, C. H. (1989). Particle-size distribution and microstructures within simulated fault gouge. *Journal of Structural Geology, 11,* 799–814.

McBeck, J., Kobchenko, M., Hall, S. A., Tudisco, E., Cordonnier, B., Meakin, P., & Renard, F. (2018). Investigating the onset of strain localization within anisotropic shale using digital volume correlation of time-resolved X-ray microtomography images. *Journal of Geophysical Research: Solid Earth.* https://doi.org/10.1029/2018JB015676.

Menéndez, B., Zhu, W., & Wong, T. F. (1996). Micromechanics of brittle faulting and cataclastic flow in Berea sandstone. *Journal of Structural Geology, 18,* 1–16.

Miller, S. A., Collettini, C., Chiaraluce, L., Cocco, M., Barchi, M., & Kaus, B. J. (2004). Aftershocks driven by a high-pressure CO_2 source at depth. *Nature, 427*(6976), 724–727.

Mirone, A., Brun, E., Gouillart, E., Tafforeau, P., & Kieffer, J. (2014). The PyHST2 hybrid distributed code for high speed tomographic reconstruction with iterative reconstruction and a priori knowledge capabilities. *Nuclear Instruments and Methods in Physics Research, Section B: Beam Interactions with Materials and Atoms, 324,* 41–48.

Mogi, K. (1971). Fracture and flow of rocks under high triaxial compression. *Journal of Geophysical Research, 76*(5), 1255–1269.

Monchiet, V., Kondo, D., Charkaluk, E., & Oana, C. (2008). Macroscopic yield criteria for plastic anisotropic materials containing spheroidal voids. *International Journal of Plasticity, 24,* 1158–1189.

Mura, T. (1982). *Micromechanics of defect in solids* (p. 588). The Hague: Martinus Nijhoff.

Nadimi, S., Fonseca, J., Bésuelle, P. & Viggiani, G. (2015). A microstructural finite element analysis of cement damage on Fontainebleau sandstone. Paper presented at the ICTMS 2015, 2nd International Conference on Tomography of Materials and Structures, 29 June–3 July 2015, Québec, Canada.

Nasseri, M. H. B., Goodfellow, S. D., Lombos, L., & Young, R. P. (2014). 3-D transport and acoustic properties of Fontainebleau sandstone during true-triaxial deformation experiments. *International Journal of Rock Mechanics and Mining Sciences, 69,* 1–18.

Otsuki, K., & Dilov, T. (2005). Evolution of hierarchical self-similar geometry of experimental fault zones: implications for seismic nucleation and earthquake size. *Journal of Geophysical Research: Solid Earth, 110,* B03303. https://doi.org/10.1029/2004JB003359.

Ougier-Simonin, A., & Zhu, W. (2013). Effects of pore fluid pressure on slip behaviors: An experimental study. *Geophysical Research Letters, 40*(11), 2619–2624.

Ougier-Simonin, A., & Zhu, W. (2015). Effect of pore pressure buildup on slowness of rupture propagation. *Journal of Geophysical Research: Solid Earth, 120*(12), 7966–7985.

Paterson, M. S., & Wong, T. F. (2005). *Experimental rock deformation-the brittle field*. Berlin: Springer.

Peng, S., & Johnson, A. M. (1972). Crack growth and faulting in cylindrical specimens of Chelmsford granite. *International Journal of Rock Mechanics and Mining Science, 9,* 37–86.

Reches, Z., & Lockner, D. A. (1994). Nucleation and growth of faults in brittle rocks. *Journal of Geophysical Research, 99,* 18159–18173.

Renard, F., Cordonnier, B., Dysthe, D. K., Boller, E., Tafforeau, P., & Rack, A. (2016). A deformation rig for synchrotron microtomography studies of geomaterials under conditions down to 10 km depth in the Earth. *Journal of Synchrotron Radiation, 23,* 1030–1034.

Renard, F., Cordonnier, B., Kobchenko, M., Kandula, N., Weiss, J., & Zhu, W. (2017). Microscale characterization of rupture nucleation unravels precursors to faulting in rocks. *Earth and Planetary Science Letters, 476,* 69–78. https://doi.org/10.1016/j.epsl.2017.08.002.

Renard, F., Weiss, J., Mathiesen, J., Ben-Zion, Y., Kandula, N., & Cordonnier, B. (2018). Critical evolution of damage toward system-size failure in crystalline rock. *Journal of Geophysical Research: Solid Earth.* https://doi.org/10.1002/2017JB014964.

Rudnicki, J. W., & Rice, J. R. (1975). Conditions for the localization of deformation in pressure-sensitive dilatant materials. *Journal of the Mechanics and Physics of Solids, 23,* 371–394.

Sadowsky, M. A., & Sternberg, E. (1949). Stress concentration around a triaxial ellipsoidal cavity. *Journal of Applied Mechanics–Transactions of the ASME, 16,* 149–157.

Sammis, C. G., & Ashby, M. F. (1986). The failure of brittle porous solids under compressive stress states. *Acta Metallurgica, 34*(3), 511–526.

Scholz, C. H. (1968). Microfracturing and the inelastic deformation of rock in compression. *Journal of Geophysical Research, 73,* 1417–1432.

Schubnel, A., Thompson, B. D., Fortin, J., Guéguen, Y., & Young, R. P. (2007). Fluid-induced rupture experiment on Fontainebleau sandstone: Premonitory activity, rupture propagation, and aftershocks. *Geophysical Research Letters, 34,* L19307.

Stanchits, S., Vinciguerra, S., & Dresen, G. (2006). Ultrasonic velocities, acoustic emission characteristics and crack damage of basalt and granite. *Pure and Applied Geophysics, 163,* 975–994.

Stavropoulou, E., Andò, E., Tengattini, A., Briffaut, M., Dufour, F., Atkins, D., et al. (2018). Liquid water uptake in unconfined Callovo Oxfordian clay-rock studied with neutron and X-ray imaging. *Acta Geotechnica.* https://doi.org/10.1007/s11440-018-0639-4.

Sulem, J., & Ouffroukh, H. (2006). Shear-banding in drained and undrained triaxial tests on a saturated sandstone; porosity and permeability evolution. *International Journal of Rock Mechanics and Mining Sciences, 43,* 292–310.

Tal, Y., Evans, B., & Mok, U. (2016). Direct observations of damage during unconfined brittle failure of Carrara marble. *Journal of Geophysical Research: Solid Earth.* https://doi.org/10.1002/2015JB012749.

Tandon, G. P., & Weng, G. J. (1986). Stress distribution in and around spheroidal inclusions and voids at finite concentration. *Journal of Applied Mechanics, 53,* 511–518.

Tapponnier, P., & Brace, W. F. (1976). Development of stress-induced microcracks in Westerly granite. *International Journal of Rock Mechanics and Mining Science and Geomechanical Abstracts, 13,* 103–112.

Tudisco, E., Andò, E., Cailletaud, R., & Hall, S. A. (2017). TomoWarp2: A local digital volume correlation code. *SoftwareX, 6,* 267–270.

Tudisco, E., Hall, S. A., Charalampidou, E. M., Kardjilov, N., Hilger, A., & Sone, H. (2015). Full-field measurements of strain localisation in sandstone by neutron tomography and 3D-volumetric digital image correlation. *Physics Procedia, 69,* 509–515.

Vasseur, J., Wadsworth, F. B., Lavallée, Y., Bell, A. F., Main, I. G., & Dingwell, D. B. (2015). Heterogeneity: The key to failure forecasting. *Scientific Reports, 5,* 13259.

Viggiani, G., Lenoir, N., Bésuelle, P., Di Michiel, M., Marello, S., Desrues, J., et al. (2004). X-ray microtomography for studying localized deformation in fine-grained geomaterials under triaxial compression. *Comptes Rendus Mécanique, 332*(10), 819–826.

Wawersik, W. R., & Fairhurst, C. (1970). A study of brittle rock fracture in laboratory compression experiments. *International Journal of Rock Mechanics and Mining Sciences and Geomechanics Abstracts, 7*(5), 561–575.

Wong, T. F., & Baud, P. (2012). The brittle-ductile transition in porous rock: A review. *Journal of Structural Geology, 44,* 25–53.

Wong, R., Chau, K., Tang, C., & Lin, P. (2001). Analysis of crack coalescence in rock-like materials containing three flaws—Part I: Experimental approach. *International Journal of Rock Mechanics and Mining Sciences, 38*(7), 909–924.

Wong, T. F., David, C., & Zhu, W. (1997). The transition from brittle faulting to cataclastic flow in porous sandstones: Mechanical deformation. *Journal of Geophysical Research: Solid Earth, 102*(B2), 3009–3025.

Wong, E., & Einstein, H. (2009). Crack coalescence in modeled gypsum and Carrara marble: Part 1. Macroscopic observations and interpretation. *Rock Mechanics and Rock Engineering, 42*(3), 475–511.

Wu, X. Y., Baud, P., & Wong, T. F. (2000). Micromechanics of compressive failure and spatial evolution of anisotropic damage in Darley Dale sandstone. *International Journal of Rock Mechanics and Mining Science, 37,* 143–160.

Zhang, J., Wong, T.-F., & Davis, D. M. (1990). Micromechanics of pressure-induced grain crushing in porous rocks. *Journal of Geophysical Research: Solid Earth, 95,* 341–352.